Mutation in the rat interleukin 34 gene impacts macrophage development, homeostasis and inflammation in the brain and periphery

Stephen Huang*[,1], Omkar L. Patkar*[,1], Sarah Schulze*[,1], Dylan Carter-Cusack[1], Susan Millard[1], Ginell Ranpura[1], Emma K. Green[1], Emma Maxwell, Gary Cowin[2], Damion Stimson[3], Nyoman D. Kurniawan[3], Sahar Keshvari[1], Rachel Allavena[4], Allison R. Pettit[1], Katharine M. Irvine[1], David A. Hume[1]

1 Mater Research Institute-UQ, Translational Research Institute, Woolloongabba, Brisbane, Australia 4102

2 National Imaging Facility, Centre for Advanced Imaging, Australian Institute for Bioengineering and Nanotechnology, The University of Queensland, St Lucia, Brisbane, Australia, 4067

3 Centre for Advanced Imaging, Australian Institute for Bioengineering and Nanotechnology, The University of Queensland, St Lucia, Brisbane, Australia, 4067

4 School of Veterinary Science, The University of Queensland, Gatton, QLD 4343, Australia

Corresponding Authors: Katharine.irvine@uq.edu.au, David.hume@uq.edu.au

Keywords: IL34, CSF1, Macrophages, CSF1R, rat immunology, Microglia

Author contributions:

SH, OLP, SS – designed the research, performed research and analysed the data. Contributed equally to this work and are co-lead authors.

DCC, SM, GR, EKG, EM, RA, GC, NK, SK, DS – performed research and analysed data.

ARP- supervised and advised the research.

DAH, KMI - designed and supervised the research, wrote the manuscript and funded the research

Conflict of interest statement

Authors declare no conflict of interest

Acknowledgements

The authors would like to thank and acknowledge the team at The University of Queensland PACE Biological resources facility (BRF) for their assistance with husbandry, maintenance, care, and monitoring of animals. We would also like to thank and acknowledge the BRF staff at the QBI animal behavioural facility and Centre for Advance imaging for the monitoring, care and maintenance of animals. The authors acknowledge the scientific and technical assistance from the microscopy, flow cytometry, and histology core facilities at Translational Research Institute and the National Imaging Facility, a National Collaborative Research Infrastructure Strategy (NCRIS) capability, at the Centre for Advanced Imaging, Australian Institute for Bioengineering and Nanotechnology, University of Queensland. We thank Glenda Gobe for advice on the renal pathology model. This work was supported by funding from Mater Foundation and NHMRC Investigator Grant #2007850 to DAH.

Abstract

Interleukin-34 (IL34) and colony stimulating factor 1 (CSF1) signal through a shared receptor (CSF1R) to control macrophage survival, differentiation and function. Here we describe the impact of loss of function mutation in the rat *Il34* gene. *Il34*$^{-/-}$ rats showed a partial reduction in macrophages within squamous epithelia (Langerhans-like cells) and in the testis. In the brain, microglia and brain-associated macrophages were selectively depleted in grey matter. A gradient of microglial density in *Il34*$^{-/-}$ cortex suggests that CSF1 can diffuse outwards from the corpus callosum. The reduced density of microglia was not associated with detectable neuropathology or behavioural alterations. In RNA-seq analysis of cortex, hippocampus and thalamus the only change is selective and uniform loss of the microglial signature. In the periphery, increased *Il34* expression has been associated with epithelial injury. In the adenine diet model of renal interstitial fibrosis both *Il34* and *Csf1* were induced. The absence of IL34 led to a significant reduction in macrophage recruitment compared to controls, but pathology assessed histologically or by detection of damage-associated mRNA signature was unaffected. We suggest that IL34 and CSF1 provide redundant signals to sustain microglia and to direct macrophage recruitment and repair tissue injury in the periphery.

51 Introduction

52 The mononuclear phagocyte system (MPS) is family of cells that includes committed hematopoietic
53 progenitors, blood monocytes and tissue resident macrophages that populate every organ in the body
54 (1-5). The proliferation, differentiation, function and survival of cells of the MPS is regulated by signals
55 from the macrophage colony-stimulating factor receptor (CSF1R). CSF1R expression is entirely
56 restricted to MPS cells and a knock-in transgenic reporter in mice highlights their abundance, location
57 and regular distribution in every organ (6). Homozygous loss of function mutations in the *CSF1R* locus
58 in mice, rats and humans are associated with depletion of MPS cells in most organs, including microglia
59 in the brain and bone-resorbing osteoclasts, and consequent severe pleiotropic impacts on postnatal
60 growth and development including osteopetrosis (7, 8). Resident tissue macrophages remain CSF1R-
61 dependent in adults and can be depleted by treatment with a blocking anti-CSF1R antibody (9).
62 CSF1R has two alternative ligands, CSF1 and IL34. Null mutations in the *Csf1* gene in mice and rats are
63 associated with tissue macrophage deficiency and osteopetrosis (10, 11). The existence of a second
64 CSF1R ligand was inferred from the age-dependent recovery of osteoclast function in CSF1-deficient
65 mice and the more severe phenotype observed in *Csf1r*$^{-/-}$ mice (12). Human IL34 was identified in 2008
66 (13). Subsequent studies revealed the functional conservation and co-evolution of the two CSF1R
67 ligands in birds (14, 15) and fish (16-19) and defined the molecular basis of binding of the two ligands
68 to the receptor (20). Although there have been several studies claiming differences in signalling
69 outcome in response to the two factors *in vitro* (21), they appear functionally equivalent *in vivo.*
70 Transgenic expression of IL34 from the *Csf1* promoter was sufficient to rescue all macrophage-
71 associated phenotypes in CSF1-deficient mice (22). In adult mice, *Il34* mRNA is expressed primarily in
72 the brain and epidermis and *Il34*$^{-/-}$ mice have a selective loss of microglia and Langerhans cells (23, 24).
73 IL34 has also been shown to regulate microglial colonisation of the brain in zebrafish (16, 18, 19). The
74 two ligands exhibit cell-specific and spatially-restricted expression in mouse brain (25); accordingly
75 administration of anti-IL34 antibody depleted microglia in grey matter whereas anti-CSF1 antibody
76 affected white matter microglia (26). Based upon conditional deletion of *Csf1* using nestin-cre, Kana

77 *et al.* (27) suggested that CSF1 was required specifically to maintain cerebellar microglia which were
78 required to regulate cerebellar development. Aside from CSF1R, IL34 has been shown to bind at least
79 3 additional putative receptors, PTPRZ1 (28), SYNDECAN1 (29) and TREM2 (30). However, at this time
80 no non-redundant biological activity of IL34 *in vivo* has been demonstrated to occur through receptors
81 other than CSF1R.
82 Increased expression of IL34 has been detected in a wide range of inflammatory diseases and
83 malignancies in patients (21, 31-43) but it remains unclear whether expression exacerbates or
84 mitigates pathology. One group has proposed that IL34 produced by regulatory T cells has a role in
85 transplant tolerance (44, 45). IL34 in mice has been implicated as an inducible mediator of tissue
86 damage in acute kidney injury (46) and in a lupus nephritis model (47). Conversely, rat models of renal
87 injury have emphasised inducible expression of CSF1 as a mediator (48, 49). Although these studies
88 have highlighted CSF1R as an anti-inflammatory drug target, CSF1 treatment actually promoted tissue
89 repair in kidney Ischaemia-reperfusion injury (50).
90 Rats have many advantages over mice as a model of human physiology and pathology (51). In terms
91 of CSF1R biology, there are clear differences in the impact of *Csf1* mutations between species. Unlike
92 *Csf1*$^{op/op}$ mice, *Csf1*$^{tl/tl}$ rats have an unremitting osteoclast deficiency and osteopetrosis but somatic
93 growth and male fertility is not affected (Reviewed in (51)). By contrast, homozygous mutation of the
94 rat *Csf1r* gene has a severe impact on postnatal growth and development (52, 53). These observations
95 suggested to us that the precise regulation and function of IL34 in control of MPS development,
96 homeostasis and immunopathology may differ between mammalian species. To investigate this
97 hypothesis, we created a null mutation in the *Il34* gene in the rat germ line. Analysis of the brain of
98 *Il34*$^{-/-}$ rats confirmed the selective loss of grey matter microglia observed with anti-IL34 treatment in
99 mice and provided evidence of haploinsufficiency. Gene expression profiling of multiple brain regions
100 indicated that there is little distinction between grey and white matter microglia, or selective gene
101 regulation by IL34. Based upon reported roles of IL34 in kidney inflammation in mice we compared
102 the response of wild-type and *Il34*$^{-/-}$ rats in a model of chronic renal injury. We conclude that IL34

103 exerts partly redundant control over recruited macrophages, but the absence of IL34 had no
104 detectable effect on either initial injury or repair. We conclude that IL34 is unlikely to be a target for
105 anti-inflammatory therapy.
106

107 ## Results

108 *Transcriptional regulation of Il34 in rats and humans*

109 Homozygous mutation of *Il34* in mice leads to selective depletion of microglia in the brain and
110 Langerhans cells in the epidermis (23, 24). Consistent with this pattern, amongst mouse tissues, *Il34*
111 is most highly-expressed in the brain and skin (see BioGPS.org). Genome-scale 5'RACE by the
112 FANTOM5 consortium revealed that expression in these two locations is driven by alternative tissue-
113 specific promoters (54). *Il34* mRNA is more widely-and uniformly expressed in human tissues (see
114 consensus data on www.proteinatlas.org) again involving separate transcription start sites (54). In
115 humans, a third TSS is utilised by a wide range of mesenchymal cell types. *Il34* mRNA is detected in
116 spleen in both humans and mice but not in lymphocytes in any state of activation (54). We recently
117 generated a transcriptional atlas for the rat by integrating 6700 RNA-seq datasets in the public domain
118 (55). We also generated a large RNA-seq dataset comparing gene expression in juvenile WT and
119 *Csf1rko* rats (56). As in humans, *Il34* mRNA is detected at comparable levels in most tissues in both
120 rat datasets; Figure S1A). To determine whether alternative promoter use was conserved, we mapped
121 RNA-seq reads from the entire rat atlas dataset to the rat genome as shown in Figure 1A**.** This analysis
122 indicated that as in mouse and human, neuronal tissues initiate transcription immediately 5' of the
123 first coding exon (CDS exon 1). In common with human, there is an alternative transcriptional start
124 site (TSS) associated with mesenchymal tissues. Skin tissue was poorly represented in the rat atlas but
125 transcripts were also detected coincident with the skin-specific 5' non-coding exon. This exon is
126 annotated on Ensembl and the sequence of the mouse skin-specific *Il34* promoter is conserved in rat
127 as well as human genomes.

128 *Phenotypic analysis of Il34$^{-/-}$ rats*

129 Since we commenced this project, Freuchet et al. (57) reported analysis of homozygous *Il34* frame-
130 shift mutation in exon 3 on an outbred Sprague-Dawley background. Their focus was on the proposed
131 function of IL34 in control of autoimmunity. They reported normal postnatal growth, reduced
132 microglia in the hippocampus, evidence of minor liver injury (marginal increase in circulating ALT, but

133 not AST or alkaline phosphatase), the presence of detectable auto-antibodies and increased
134 circulating CSF1. They also reported a selective reduction in $CD8^+$ T cells in the spleen.
135 The *Il34*$^{-/-}$rats on the inbred Fischer 344 background were generated by deletion of the 134bp second
136 coding exon using CRISPR-Cas9 (Figure S1F**)**. This deletion removes 35 amino acids of the active IL34
137 protein and introduces an in-frame stop codon at the start of the next exon. *Il34*$^{-/-}$ rats were born at
138 the expected Mendelian ratios. Although *Il34* mRNA is highly expressed by osteoblasts (55), as
139 reported previously (57) there was no significant impact of the *Il34* mutation on bone density
140 detectable by micro-computed tomography (μCT) (Figure 1B), by contrast to the severe unremitting
141 osteopetrosis observed in *Csf1*$^{tl/tl}$ rats (11). Unlike *Csf1r*$^{-/-}$ (52) and *Csf1*$^{-/-}$ (11) rats, postnatal somatic
142 growth was not affected in *Il34*$^{-/-}$ rats (Figure 1C), male-specific growth advantage post sexual maturity
143 was preserved and both males and females were fertile. *Csf1r*$^{-/-}$ rats have a partial loss of red pulp
144 macrophages in the spleen and complete absence of marginal zone ($CD169^+$) and marginal metallophil
145 ($CD209B^+$) populations, which are CSF1-dependent in mice (53). In the *Csf1r*$^{-/-}$ liver, Kupffer cells are
146 reduced by around 70% and the pericapsular macrophage population is absent (52). We found no
147 significant impact of IL34 deficiency on either liver population. In contrast to mouse, *Il34* mRNA is
148 highly-expressed in rat spleen (55). Splenic white matter topology and the location and abundance of
149 $IBA1^+$ and $CD209b^+$ macrophage populations was unaffected by the lack of IL34 **(**Figure 1D&E**)**. Given
150 the widespread expression of *Il34* mRNA we considered whether the absence might influence CSF1
151 homeostasis. Circulating CSF1 is regulated primarily by receptor-mediated endocytosis and
152 degradation by macrophages and is elevated in *Csf1r*$^{-/-}$ rats (52). However, serum CSF1 levels were
153 not altered in *Il34*$^{-/-}$ rats (Figure 1F).
154 Analysis of bone marrow, blood and spleen by Flow Cytometry revealed no significant differences in
155 the relative frequency of T cell, B cells, blood monocytes or granulocytes (Figure 1G, Figures S1B) in
156 *Il34*$^{-/-}$ rats compared to WT. In contrast to Freuchet et al, *Il34*$^{-/-}$ rats had a normal distribution of B cells,
157 CD4 and CD8 T cells in lymphoid organs, including spleen, thymus and cervical lymph node (Figure

158 S1C-E). These data indicate that the hematopoietic phenotype seen in the rat *Csf1r* mutation (52) is
159 also primarily due to loss of CSF1 rather than IL34 signalling.
160 To assess the effect of the IL34 knockout on tissue macrophage populations we crossed the mutation
161 to the *Csf1r*-mApple transgenic reporter line, which is expressed in all tissue macrophages and at lower
162 levels in granulocytes and B cells (58, 59). No gross differences in the distribution of tissue
163 macrophages were observed by wholemount imaging in any organ, including those in which *Il34*
164 mRNA is highly-expressed such as connective tissue, gut, muscle and thymus (55) (Figure 1H, Figure
165 S1F). By contrast to the reported loss of Langerhans cells in *Il34*$^{-/-}$ mice(23, 60), in *Il34*$^{-/-}$ rats there was
166 only partial reduction in the apparent density of Langerhans cells in stratified epithelia of the ear,
167 tongue, oesophagus and foot in adult and *Il34*$^{-/-}$ rats and the morphology was unaffected (Figure 2A).
168 Aside from the brain (see below), the only other location where we detected a clear loss of a
169 macrophage subpopulation was the testis, which contains three topologically-distinct populations,
170 interstitial and peritubular macrophages as described in the mouse (61-63) and a distinct
171 surface/subcapsular population. The surface and peritubular populations were relatively depleted in
172 *Il34*$^{-/-}$ rats (Figure 2B). Their loss is more readily appreciated through visualisation of 3 dimensional Z
173 stacks (Supplemental video files 1-2).
174 *The effect of Il34 mutation on microglial density, location and gene expression*
175 The brain contains two distinct populations of mononuclear phagocytes, classical microglia and brain-
176 associated macrophages (64) that line the vasculature and brain surfaces. Flow cytometry analysis of
177 leukocyte populations in disaggregated brain revealed that microglia (CD45^{low}/Cd11b/c^{high}) and brain-
178 associated macrophages (CD45^{high}/CD11b/c^{low}) were both significantly reduced in the *Il34*$^{-/-}$ brain
179 (Figure 2C). The relative abundance of both populations was reduced to a similar extent in
180 heterozygotes (*Il34*$^{+/-}$) indicating a lack of dosage compensation.
181 We next performed immunofluorescent staining on free floating sections to assess the morphology
182 and precise location of microglia in specific brain subregions. Figure 3A/Figure S2A show
183 representative images and Figure 3B/Figure S2B show quantitative analysis of IBA1^{+} cells in WT, *Il34*$^{+/-}$

184 and *Il34*$^{-/-}$ brains. There is clear depletion of classical highly-ramified microglia in defined grey matter
185 regions in IL34-deficient brain. The remaining microglia have a distinct morphology, apparently
186 aligned along the fibre tracts. This is particularly evident in the striatum. Interestingly, although the
187 global impact of IL34 deficiency in the cerebellum and brain stem is less obvious, ramified microglia
188 were clearly reduced. Consistent with the analysis in Figure 2, Figure 3 shows that microglial density
189 in multiple brain regions of *Il34*$^{+/-}$ rats was intermediate between wild-type and *Il34*$^{-/-}$ animals. The
190 microglia in this case remained evenly spaced but at a lower density. Figure 4A shows the density of
191 microglia in the multiple layers of the cortex from the corpus callosum to the meninges in the three
192 genotypes. In the *Il34*$^{-/-}$ brain, we noted an apparent outward gradient of microglial and perivascular
193 macrophage loss.
194 To confirm the conclusion from the Flow Cytometry profile that microglia and brain-associated
195 macrophages (BAM) were equally affected by the loss of IL34, we located the BAM marker CD163 (65)
196 on sections of cortex from wild type and *Il34*$^{-/-}$ brain. Figure 4B-F shows the selective loss of CD163^{+}
197 cells from the grey matter regions where microglia were also reduced but not from the meninges.
198 Taken together, the data demonstrate that IL34 and CSF1 are only partly compartmentalised within
199 the brain, each contributing to the local sustainable CSF1R-dependent mononuclear phagocyte
200 population.
201 To analyse the molecular consequences of microglial deficiency we profiled gene expression in the
202 cortex, hippocampus and thalamus of WT and *Il34*$^{-/-}$ rats at 10 weeks of age. The data are provided in
203 Table S1**.** Surprisingly, *Il34* mRNA is still detectable, reduced by around 50% in the mutant rats.
204 Mapping of the primary RNA-seq data to the rat genome confirmed the removal of the second coding
205 exon and generation of a spliced non-coding transcript that presumably does not undergo nonsense-
206 mediated decay.
207 Consistent with the loss of IBA1 staining in sections, *Aif1* mRNA was reduced by 40% in hippocampus
208 and thalamus and 60% in cortex. As in previous analysis of brain regions in *Csf1r*$^{-/-}$ rats (66) the
209 complete dataset was subjected to network analysis using *Graphia* to identify clusters of co-expressed

210 transcripts (Table S1). The only cluster clearly associated with IL34 genotype, Cluster 18, contains 80
211 transcripts including *Aif1* and *Csf1r* and overlaps with the microglial signature identified previously in
212 comparison of WT and *Csf1r*$^{-/-}$ rats (66). Figure 5A shows the average expression of genes within this
213 cluster, reduced by 40-60% in each brain region, which parallels the loss of *Aif1* and IBA1. We did not
214 detect expression of markers of damage-associated microglia (e.g *Clec7a*) or the loss of homeostatic
215 markers reported in *Il34*$^{-/-}$ mice (27, 67). Figure 5B shows the detection of individual transcripts,
216 confirming that homeostatic markers such as *P2ry12* and *Tmem119* were reduced to the same extent
217 as *Aif1, Csf1r, C1qa* and *Itgam.* Colocalisation of IBA1 and TMEM119 in cortex confirmed that the level
218 of expression in individual microglia is unchanged in the *Il34*$^{-/-}$ brain. (Figure 5C). Cluster 18 includes
219 three transcription factor genes, *Spi1, Irf5* and *Irf8,* but excludes *Sall1*, which is required for microglial
220 lineage identity (68, 69) (Figure 5D**).** Analysis of *Csf1r*$^{-/-}$ rat brains indicated that *Sall1* is not microglia-
221 restricted (66). Markers of brain-associated macrophages are more difficult to detect in total RNA-seq
222 data, but *Cd74* and *Cd68* were also reduced in *Il34*$^{-/-}$ brains. Separate sheets in Table S1 show
223 transcripts ranked based on IL34KO/WT ratio with known CSF1R-dependent microglia or macrophage-
224 associated transcripts highlighted.
225 In overview, the data demonstrate that the transcriptomic profiles of IL34-independent (i.e. CSF1-
226 dependent) microglial and BAM populations do not differ significantly from those of IL34-dependent
227 populations located mainly in grey matter.
228 *The effect of microglia deficiency on brain development and behaviour*
229 Dominant or recessive *CSF1R* mutations in humans are associated with microglial deficiency and
230 consequent neuropathology (70). By contrast to *Csf1r*$^{-/-}$ rat brains, the *Il34*$^{-/-}$ brains showed no
231 evidence of ventricular enlargement and the transcriptomic profiles did not include the induction of
232 stress response genes (e.g. *Rbm3, Mt1/2*) reported in the brains of juvenile *Csf1r*$^{-/-}$ rats (66) (Figure
233 S3A). In the hippocampus of *Csf1r*$^{-/-}$ rats we observed disorganised maturation of neuronal progenitors
234 stained with the marker doublecortin (DCX) but considered that this might be a consequence of stress
235 due to ventricular enlargement (66). Although microglia are depleted in the vicinity of the dentate

236 gyrus in *Il34*$^{-/-}$ brains, DCX staining did not distinguish wild type and mutant animals (Figure S3B, S3C).
237 Furthermore, in common with previous analysis of *Csf1r*$^{-/-}$ rat brains, the expression profiling did not
238 reveal any effect of the loss of grey matter microglia on astrocytes. The expression of *Gfap* mRNA and
239 the density, distribution and morphology of GFAP^{+} astrocytes was not affected by microglia deficiency
240 (Figure S3D&E).
241 One advantage of the rat is the wide range of human-relevant behaviour and functional tests
242 compared to mice (71). We subjected WT, *Il34*$^{+/-}$ and *Il34*$^{-/-}$ male and female rats to a battery of tests
243 between 4 and 6 months of age. We found no significant differences in performance in the sucrose
244 preference, O maze, open field and novel object recognition tests (Figure S4).
245 To look for age-dependent pathology resembling human leukodystrophy or neurodegeneration, we
246 analysed the same cohort at 18 months of age. Quantification of IBA1^{+} cells demonstrated that the
247 selective loss of microglia in cortex, hippocampus and thalamus in *Il34*$^{-/-}$ and partial depletion in *Il34*$^{+/-}$
248 rats was still present at 18 months (Figure S5A&B). Astrocytosis detectable by GFAP staining can be a
249 sensitive indicator of neuropathology, accelerated in microglia-deficient mice (72, 73). However, the
250 density and morphology of GFAP^{+} astrocytes remain unchanged in any brain region in the aged animals
251 (Figure S5C&D). In the cluster analysis, as a consequence of sample-to-sample variation in myelination,
252 oligodendrocyte-specific transcripts (e.g. *Olig1, Mbp*) form part of a single cluster, Cluster 6, that is
253 not correlated with *Il34* genotype. Diffusion tensor imaging revealed no significant effect of the lack
254 of IL34 on any white matter structure or the overall volume of any brain region (Figure S3F, Table S2).
255 Notably, there was no ventricular enlargement and no detectable flares in the thalamus suggestive of
256 calcification at this age. In addition, we assessed [^{18}F]DPA714 uptake by PET/MR to measure
257 neuroinflammation (74). This radioligand binds specifically to TSPO, a mitochondrial membrane
258 protein, and is used to detect neuroinflammation in human patients (74-79). We focussed analysis on
259 the hippocampus, thalamus, pituitary and different cortex regions. We detected differences in uptake
260 between male and female animals consistent with previous reports (80) and a male specific increase

261 in uptake with age. However, there was no detectable difference in uptake between genotypes (Table
262 S3).
263 Recent studies have highlighted the relationship between microglial dyshomeostasis and the loss of
264 perineuronal nets (PNN) associated with cortical parvalbumin interneurons (81, 82). Proteoglycans
265 within these extracellular matrix structures can be detected by staining with *Wisteria floribunda*
266 *agglutinin* (WFA) and we localized parvalbumin (PV) neurons in the cortex. We found no significant
267 difference in WFA or PV staining between WT and IL34$^{-/-}$ rats (Figure S5E&F). Microglia-deficiency in
268 mice leads to reactive astrocytosis and extensive calcification in the thalamus detectable by 3-6
269 months of age and progressing in severity (83, 84). Consistent with the lack of detectable astrocytosis
270 in the thalamus of aged *Il34*$^{-/-}$ rats there was no calcification detectable by labelled risedronate staining
271 (**Data not shown**). In summary, the only significant difference detected between WT and *Il34*$^{-/-}$ brains
272 at any age examined is the selective loss of microglia in grey matter and associated reduction in
273 detectable microglia-specific transcripts.
274 **The role of IL34 in chronic inflammation in the kidney**
275 Network analysis of individual tissues with multiple region or state-specific RNA-seq data revealed a
276 strong correlation between *Il34* mRNA and a macrophage-specific signature in the kidney (55)
277 suggesting that IL34 does contribute to control of resident macrophage abundance in this organ. To
278 determine the role of IL34 in chronic renal inflammation, we established the rat adenine diet model
279 (85, 86), which leads to slowly progressive kidney damage with many features of chronic kidney
280 disease in humans including tubular atrophy, interstitial fibrosis and glomerulosclerosis. We exposed
281 cohorts of equal numbers of male and female WT and *Il34*$^{-/-}$ rats to an 0.2% adenine diet or normal
282 chow for 6 weeks. Both WT and *Il34*$^{-/-}$ rats had normal growth when placed on the adenine diet (Figure
283 6A). At a cage level, increased water consumption was evident by two weeks and by 5 weeks was more
284 than doubled for both male and female cages (Figure 6B&C). As reported previously (86) the effect of
285 the diet on renal function was gender-dependent. In males we detected increased serum creatinine

286 and blood urea nitrogen, whereas serum metabolites were not affected in females. These changes
287 were not significantly reduced in the *Il34*$^{-/-}$ males (Figure 6D&E).
288 A feature of the pathology in this model is the deposition of adenine crystals in the cortex, which
289 appeared reduced in females regardless of genotype, thickening of Bowman's capsule and mesangium
290 in glomeruli, loss of tubular brush borders; tubular atrophy and dilatation, expansion of interstitial
291 mononuclear cell populations and extensive fibrosis detected with Sirius Red (Figure 6F&G & Figure
292 S6). Glomerular pathology appeared male-specific perhaps associated with the observed gender
293 difference in clearance function. Quantitative analysis did not reveal any significant effects of the *Il34*
294 mutation, notably including the extensive interstitial fibrosis (Figure 6F&G).
295 We next asked whether the loss of IL34 had any effect on renal macrophage populations. Renal
296 macrophages can be detected by staining for IBA1 and IBA1^{+} cells are completely absent in the kidneys
297 of *Csf1r*$^{-/-}$ rats (52). There was a massive expansion of IBA1^{+} macrophage populations in the cortex and
298 medulla of rats on the adenine diet (Figure 7A&7B). Within the limits of quantification, the density of
299 renal IBA1^{+} cells in control animals was not significantly affected by the loss of IL34 but the response
300 to the adenine diet was reduced by around 50% (Figure 7D&7E). The presence of macrophages
301 expressing the haptoglobin receptor, CD163, has been associated with kidney injury in both animal
302 models and human disease and is commonly considered a marker of an anti-inflammatory phenotype
303 (87). In the adenine model, we detected expansion of a CD163^{+} cell population in the medulla only
304 which was significantly reduced in *Il34*$^{-/-}$ rats (Figure 7C&7F).
305 To further analyse the effect of the IL34 knockout on renal pathology, we performed total RNA-Seq
306 analysis of kidneys from wild-type and *Il34*$^{-/-}$ male control and adenine-fed rats. The complete dataset
307 is provided in Table S4**.** Separate Tabs show ranked lists of average expression comparing control
308 versus adenine-fed for each genotype and wild-type versus *Il34*$^{-/-}$ for the adenine-fed and control
309 animals. Table S4 also includes a highlights tab showing the data for selected adenine-regulated genes
310 in different functional groups that provide markers of pathology and an indication of the impact of the
311 *Il34* mutation. *Csf1* and *Il34* mRNA were each detectable in control kidney and increased >2 fold in

312 response to the adenine diet. Consistent with the reduced detection of IBA1^{+} cells *in situ*, the detection
313 of *Aif1* mRNA was increased ~6.5 fold in the kidneys of adenine-treated rats and this increase was
314 reduced significantly in the *Il34*$^{-/-}$ rats. Network analysis of the complete dataset is also shown in Table
315 S4**.** This analysis revealed a large cluster of 5879 transcripts (**Cluster 1**) with a shared pattern of up-
316 regulation in response to the adenine diet regardless of genotype, with a trend toward lower
317 expression in the *Il34*$^{-/-}$ rats. We recently identified the kidney resident macrophage signature by
318 comparing the transcriptional profiles of kidney from wild-type and *Csf1r*$^{-/-}$ rats (56). 158/166 CSF1R-
319 dependent transcripts identified by that analysis are contained within **Cluster 1** and are highlighted in
320 Red in Table S4**.** These transcripts were increased 4-40 fold in the kidney on the adenine diet and
321 reduced in *Il34*$^{-/-}$ rats compared to wild-type (ratio 0.27-0.68; mean 0.46). The individual data for
322 selected macrophage genes *Aif1, Adgre1, Csf1r, Clec10a, Mrc1 a*nd *C1qa* are shown in Figure S7A*.* One
323 other feature evident in Cluster 1 is the transcriptional signature of the cell division cycle. The cluster
324 contains 267/496 genes with known functions in the cell cycle (88) including *Mki67*. The overall
325 pattern indicates that the response to adenine involves expansion of macrophage populations with a
326 resident transcriptomic profile and that this expansion depends in part on induction of IL34. *Csf1* and
327 *Il34* are not the only inducible transcripts encoding myeloid growth factors in the injured kidney. *Ftl3lg*
328 mRNA was detected at a similar level and increased in response to adenine, likely driving expansion
329 of FLT3-expresssing classical dendritic cells (cDC1) and increased detection of markers *Flt3, Ccr7, Xcr1,*
330 *Itgae* and *Clec9a* (89) (Figure S7B). Although macrophages appear to be the dominant inflammatory
331 cell population, **Cluster 1** also includes numerous chemokines and signature genes indicating
332 recruitment of monocytes (*Cd14, Cyba*), T cells (*Cd3e/d/g*), and granulocytes (*S100a8/9*), each also
333 reduced in the *Il34*$^{-/-}$*.*
334 The tubular pathology and interstitial fibrosis observed in tissue sections is associated with markedly
335 increased detection of markers of epithelial injury including cytokeratins (*Krt7/8/18/19* (90)), *Havcr1*
336 (aka Kidney Injury Marker 1), *Spp1* (osteopontin) and *Mmp7* (91) and of myofibroblasts (e.g. *Acta2,*
337 *Col4a1, Mgp*). Cytokines *Il19* and *Il24,* implicated in epithelial injury and fibrosis in human kidney

338 disease and in mouse models (92, 93) were almost undetectable in control and strongly-expressed in
339 diseased kidney. Consistent with evidence of inflammasome activation in crystal-induced
340 nephropathy (94), *Il1b* and *Il18* were each increased. Epithelial loss or dysfunction is indicated by
341 reduced detection of tubule markers such as *Umod, Slc12a1* and *Slc21a4* defined in the rat
342 transcriptomic atlas (55). Within the constraints of inter-individual variation, there was no significant
343 difference in detection of any of these markers of pathology between the wild-type and *Il34*$^{-/-}$ rats on
344 the adenine diet (Table S4).
345 The histopathology and RNA-seq analysis indicate that IL34-dependent expansion of resident
346 macrophages is not a driver of tubular damage or fibrosis. The alternative possibility is that it is a
347 response to injury and associated with repair. To address this possibility, we looked at recovery from
348 the adenine diet. Wild type and *Il34*$^{-/-}$ rats were fed the diet for 6 weeks then transferred to normal
349 chow for 4 weeks. Following transfer to normal chow, both groups continued to grow normally. Serum
350 creatinine and BUN trended downwards towards control levels but remained elevated independent
351 of genotype (Figure S8A&B). The expression of *Cd163* mRNA in wild-type animals returned to baseline
352 and fibrosis scores based upon Sirius red staining also showed evidence of recovery but there was no
353 difference between wild-type and *Il34*$^{-/-}$ rats (Figure S8C&D). In summary, the adenine-induced renal
354 pathology was slowly reversed following removal of the diet but reversal was not altered by the
355 absence of IL34.
356

357 Discussion

358 A previous analysis of the phenotype of an *Il34* mutation in rats (57) was focussed on the putative
359 expression of IL34 by regulatory T cells (Treg) and a role in autoimmunity (44, 45). The expression of
360 *IL34* mRNA reported in rat and human T cells was detected by qRT-PCR and in humans by Flow
361 Cytometry. The conclusion that IL34 is a T cell lymphokine is not supported by other evidence. *IL34*
362 mRNA is not detectable in human Treg in bulk (54, 95) or single cell RNA-seq data (96) and was not
363 detected in either CD4 or CD8 rat Treg isolated using a *Foxp3*-EGFP reporter by the same group (97).
364 We were not able to reproduce the apparent loss of CD8 T cells reported in *Il34*$^{-/-}$ rats (57). Indeed, we
365 found no detectable effect on leukocyte populations in the steady state. Similarly, no change in
366 relative abundance of T cell populations was detected in *Il34*$^{-/-}$ mice (24).

367 In mice, *Il34* mRNA is expressed selectively in epidermis and brain, whereas *Csf1* is expressed in
368 mesenchymal cells and undetectable in epidermis (biogps.org). By contrast, in rats *Il34* mRNA is widely
369 expressed. In the rat skin *Il34* and *Csf1* mRNA are expressed at similar levels (biogps.org/ratatlas)
370 although the separation of dermis and epidermis has not been reported. In the mouse, Langerhans
371 cells in the epidermis of the ear were almost entirely IL34-dependent (23, 24). Other squamous
372 epithelia were not examined. In the *Il34*$^{-/-}$ rat, intraepithelial Langerhans-like cells in squamous
373 epithelia were only partly depleted compared to WT (Figure 2A).

374 The main location where the loss of IL34 impacted resident tissue MPS populations is the brain. A
375 detailed analysis of microglial location and morphology in mice (98) indicated the relatively low
376 density of F4/80^{+} cells in white matter and fibre tracts, and the unique morphology aligned along the
377 fibres. In common with humans (99), microglia in rat brain are equally abundant in white and grey
378 matter, but in white matter they have the same elongated morphology described in mice. Consistent
379 with the reported effect of anti-IL34 and anti-CSF1 treatment in adult mice (26), we observed selective
380 loss of microglia in grey matter in *Il34*$^{-/-}$ rats but the effect was subtle. Within the grey matter regions,
381 CD163^{+} perivascular macrophages were also depleted but the remaining IBA1^{+} cells occupied a distinct
382 location. Because of their relative abundance, the retention of morphologically distinct microglia,

383 elongated along the fibre tracts, is obvious in the rat especially in the striatum. In comparison to rats,
384 the *Il34* mutation in mice had a greater overall impact on microglial density, including a reduced
385 density in the corpus callosum, and the residual microglia were not morphologically distinct (23, 24).
386 Kana *et al.* (27) reported the impact of conditional *Csf1* deletion in mouse brain which produced
387 selective microglial depletion in the cerebellum. Although *Csf1* is more highly-expressed in the rat
388 cerebellum than *Il34,* there was also selective loss of microglia within grey matter in this region and in
389 the brain stem in the *Il34*$^{-/-}$ rats (Figure 3). This was not detected in *Il34*$^{-/-}$ mice (23, 24). Finally, we
390 report for the first time that IL34 deficiency is not dosage compensated and *Il34*$^{+/-}$ rats have a partial
391 loss of grey matter microglia. In common with the reduced density of microglia in mice with a
392 heterozygous dominant-negative *Csf1r* mutation (100) the residual microglia in the *Il34*$^{-/-}$ rat brain are
393 evenly spaced. The regular distribution of macrophages in tissues has been attributed to competition
394 for growth factors and mutual repulsion, so that macrophages (including microglia) are autonomous
395 and occupy a territory rather than a precise niche (2). The strict compartmentalisation of IL34 and
396 CSF1 implied from analysis of *Il34*$^{-/-}$ mice (23, 24) is clearly not the case in the rat. The gradient of
397 microglial loss observed in the cortex (Figure 4A) suggests that CSF1 produced in corpus callosum is
398 able to diffuse outward to partly compensate for the loss of IL34 (101).
399 The expression profiling of the brain of *Il34*$^{-/-}$ rats revealed the coordinated partial loss of microglia-
400 associated signature transcripts previously identified as CSF1R-dependent from analysis of multiple
401 brain regions in *Csf1r*$^{-/-}$ rats (66). The thalamus was included because of recent evidence that the loss
402 of microglia in mice leads to calcification of this brain region (83, 84). Aside from the loss of the
403 microglial signature, we did not detect significant changes in expression of any transcripts that would
404 indicate either a neurodevelopmental defect or pathology. This observation provides evidence against
405 a CSF1R-independent function of IL34 mediated through binding to PTPRZ1, which is expressed
406 specifically by neurons (28). The absence of microglia in mice with a hypomorphic *Csf1r* mutation also
407 leads to progressive demyelination, which has been analysed as a model for leukodystrophy
408 associated with human *CSF1R* mutation (83, 102). Not surprisingly, since white matter microglia are

409 largely spared, we did not detect changes in myelin in the *Il34*$^{-/-}$ rat. Whilst it is difficult to prove the
410 absence of an effect, *Il34*$^{-/-}$ rats were not distinguishable from wild-type littermates in brain imaging
411 and in a wide range of behavioural tests. Similarly, the density of perineuronal nets, a morphological
412 surrogate for neuronal plasticity in the cortex that is regulated by microglia in mice (81, 103) was not
413 altered in *Il34*$^{-/-}$ rats. In overview, the analysis supports the view that microglial functions in
414 neurodevelopment are redundant (66, 104). Their clear essential function in mice is in the mitigation
415 of neuropathology (23, 24, 72, 73, 83, 102, 105). Interestingly, a relatively common stop-gain mutation
416 in human *IL34* (Y213Ter, minor allele frequency ca. 0.1) has been associated with an increased relative
417 risk of developing Alzheimer's disease (106). This variant lies downstream of the active IL34 peptide,
418 so the functional impact on active IL34 generation is not known. IL34 amino acid sequence is highly
419 conserved in mammals and birds (15) but available human exome sequences
420 (https://gnomad.broadinstitute.org/) highlight multiple coding variants within the active peptide in
421 human populations. The lack of dosage compensation and partial loss of microglia in *Il34*$^{+/-}$ rats
422 indicates that heterozygous loss of function *IL34* mutation could impact microglia in humans. Equally,
423 since homozygous mutants are viable, long-lived and fertile, homozygous loss of function in humans
424 may be tolerated. The *Il34*$^{-/-}$ rat provides a model in which to dissect the specific functions of microglia
425 that more closely approximates human biology.
426 The emerging literature on IL34 views it as a pro-inflammatory cytokine and therefore a potential
427 target in inflammatory disease (21, 42). Whilst there is clear evidence of an association between
428 increased detection of IL34 and disease severity in a range of human inflammatory diseases, evidence
429 of function is more equivocal and almost entirely based on mouse models. For example, Baek *et al.*
430 (46) reported that IL34 generated by tubular epithelial cells (TECs) promoted macrophage-mediated
431 acute epithelial injury in a kidney ischemia reperfusion model and exacerbated subsequent chronic
432 fibrotic disease. This report is difficult to reconcile with the trophic effects of the alternative CSF1R
433 ligand, CSF1, in the same model (50). Our comparative analysis of chronic renal injury in the wild-type
434 and *Il34*$^{-/-}$ rats does not support the view that IL34 is an essential mediator of tissue injury. In wild-

435 type rats in the adenine model we detected induction of both *Il34* and *Csf1* mRNA, increased
436 abundance of interstitial macrophages, and increased detection of numerous transcripts expressed
437 specifically by resident kidney macrophage populations. Previous studies have demonstrated that
438 inducible expression of CSF1 drives local macrophage proliferation in response to renal injury in rats
439 (48, 49). The relative density of IBA1^{+} cells, and detection of resident macrophage-associated
440 transcripts, was approximately halved in the *Il34*$^{-/-}$ rats. The simplest explanation is that the two
441 inducible CSF1R agonists are partly redundant. FLT3-ligand may also contribute to expansion of
442 interstitial mononuclear phagocyte populations. We observed increased expression of *Flt3lg* mRNA
443 and of transcripts associated with classical dendritic cells in response to the adenine diet (Table S4)
444 There has been significant debate in the literature as to whether to classify renal interstitial myeloid
445 populations as macrophages or DC based on surface markers (89, 107). Interestingly, expression
446 profiling of kidneys of *Csf1r*$^{-/-}$ rats revealed 80% loss of *Flt3* mRNA suggesting that renal interstitial
447 myeloid cells may be unique in expressing both FLT3 and CSF1R (56).
448 Whereas the absence of IL34 compromised interstitial macrophage expansion in the injured kidney
449 (Figure 7), it had no significant impact on any aspect of pathology, including clearance functions, overt
450 pathology or the expression of damage-associated transcripts (Table S4). Furthermore, the slow
451 recovery following removal of the adenine diet was neither prevented nor accelerated. CSF1 and IL34
452 are also both induced following epithelial injury in the intestine, including in human ulcerative colitis
453 (43). In both rats and mice, IL34 deficiency caused a moderate increase in pathology in the dextran
454 sodium sulphate colitis model (43, 57, 108). Taking all of the evidence together, we suggest that
455 increased expression of CSF1R ligands is a consequence rather than a cause of pathology associated
456 with chronic tissue injury that serves to promote resolution. That conclusion would imply that
457 treatment with antagonists of either ligand or the receptor is unlikely to be therapeutic in
458 inflammatory disease and may actually exacerbate or prolong the injury.
459

460 ## Methods and Materials

461 *Sex as a biological variable*

462 Both male and female animals were used unless otherwise stated.

463 *Animals*

464 IL34 knockout rats were generated under contract by Taconic Biosciences (Germantown, NY, US)
465 through CRISPR mediated recombination with guide RNAs flanking exon 2 of the *Il34* gene (Figure
466 S1G). Animals carrying the knockout allele were imported to Australia, rederived into a specified
467 pathogen-free (SPF) facility and maintained on the F344/DuCRL background. Deletion of exon 2 was
468 confirmed by PCR using flanking primers (5'TTTAGCATCTCAGAGCCATCAG (forward),
469 5'GCAGCTTGACAACAGACAGG (reverse) giving products of 1541bp (WT) and 353bp (Mut). The same
470 primers were used for genotyping.

471 There are no gross morphological differences in the IL34 homozygous or heterozygous animals and
472 both male and female animals are fertile. Rats between 8-10 weeks of age were used to characterize
473 distribution and morphology of macrophages unless stated otherwise. Rats for behavioural tests were
474 4 months of age at the time of behavioural testing and 6 months of age for PET/MR scanning. A cohort
475 of animals were aged a minimum of 18 months (18-26 months) and also underwent PET/MR scanning.
476 For whole mount imaging, *Il34*$^{-/-}$ rats were crossed with the *Csf1r*-mApple transgenic reporter line (58).
477 F1 progeny were interbred and F2 animals 8-10 weeks of age were used for analysis.

478 All animals were housed in ventilated cages at 21°C at a relative humidity of 76% and provided
479 standard chow and water *Ad libitum*. All animal procedures were performed at The University of
480 Queensland under protocols approved by the Institutional Animal Ethics Unit (UQ AE2022/000676,
481 AE2021/000337, AE2022/00066, and AE2022/000191).

482 *Adenine induced chronic kidney injury model*

483 Rats were 6 weeks of age at the beginning of the adenine diet. Adenine treated rats received R&M
484 0.2% Adenine Normal Feed (SF14-139, Specialty Feeds, Glen Forrest, WA) and water *Ad libitum* for 6

weeks while control animals were kept on standard chow. The recovery cohort also received adenine for 6 weeks and then were given standard chow for4 weeks.

Animal behaviour studies

Sucrose preference test

Animals were housed individually for 1 week prior to testing. A two bottle paradigm was set up for each cage with one bottle containing standard water and the second containing a 5% sucrose solution diluted in the standard drinking water. Bottles were weighed prior to testing and after removal. Animals began testing at 6pm each evening and bottles were replaced with standard water the following morning at 6am and animals were tested again between 6pm-6am with bottle positions swapped.

Open field test

Animals were placed in the centre of a 56cm square arena and allowed to explore for 10 minutes. A border 10cm from the edge was considered the border boundary and the remaining space within the square was considered the central area. Time spent within the central area was quantified when the centre of the animal's body occupied this space.

Novel object recognition

Novel object recognition assays were performed in a 112x56cm arena. Two pyramidal objects were placed 26cm from the edges of the arena for the learning phase which occurred over 2 days. Animals were placed in the centre of the arena and allowed to explore for 10 minutes. On the third day one object was replaced with an ellipsoid-shaped object and animals were placed in the centre and allowed to explore for 10 minutes. Time interacting with objects was quantified when the nose of the animal was within the boundaries of each object.

Elevated O-maze

The platform is a circular disc approximately 120cm in diameter. The platform width was approximately 10cm and elevated 60cm above the ground. The closed arms of the O-maze consisted

510 of walls that were 30cm tall. Animals were placed in the centre of the open arms and allowed to
511 explore for 10 minutes. Total animal movement and time spent in the open arms were quantified.

512 *MicroCT analysis of bone*

513 Whole right hind limbs were fixed in 4%PFA/PBS for 6 days at 4°C and then transferred into PBS and
514 scanned using Bruker SkyScan 1272. All x-ray projections were reconstructed in a blinded manner
515 using a modified back-projection reconstruction algorithm (NRecon 1.7.3.1 software (SkyScan; Bruker
516 µCT) to create cross-sectional images, and 3-dimensional (3D) reconstructions were viewed using
517 CTvox 3.3.0 (Bruker µCT). Reconstructed images were then analyzed using CTAn 1.19 software
518 (Bruker), which has inherent 2D and 3D analysis tools (109).

519 *Flow cytometry and haematology*

520 Blood was collected via cardiac puncture into EDTA coated minicollect tubes (Greiner, #450532) for
521 haematology or serum separator vacuette tubes (Greiner, #456010) for sera analysis. 100uL of blood
522 was treated with 1ml of red blood cell lysis buffer (0.15M NH4Cl, 10mM NaHCO3) for 2 minutes at
523 room temperature then washed in 10mL of PBS. Lysed preparations were then spun at 500g 5min 4C,
524 washed in 10mL of PBS and then resuspended in FACS buffer. Thymus, cervical lymph nodes (cLN),
525 spleen and bone marrow were collected in FACS buffer (2%FCS/PBS) and filtered through a 40 µM
526 filter to produce single cell suspension. Splenic cell preparations were treated with red blood cell lysis
527 buffer. All single cell preparations were enumerated and $1x10^6$ cells were stained for 30min at 4°C.
528 Brain tissue for flow cytometry was collected from one hemisphere by performing a sagittal incision
529 down the midline of the brain. This tissue was then minced with a scalpel in a petri dish, resuspended
530 in HBSS containing collagenase type IV (1mg/mL), dispase (0.1mg/mL), and DNase1 (19mg/mL), and
531 incubated on a rocking platform for 45 min at 37°C. The tissue was then passed through a 70µm filter,
532 washed in 25mL PBS and centrifuged (at 400g and 4°C for 5 min). Supernatant was removed and the
533 pellet resuspended in 12.5mL isotonic Percoll (2.44mL Percoll (Cytiva, MA, USA), 0.47mL 10x PBS,
534 7.815mL 1x PBS). The suspension was centrifuged at 800g for 45 min (no brake) at 4°C. The

535 supernatant containing the top myelin layer was aspirated, and the pellet was washed twice with PBS,
536 and finally resuspended in flow cytometry (FC) buffer (PBS/2% FCS).
537 The following antibody panel was used across tissue preparations:

	Panel 1	Panel 2
Antibodies	CD32 HIS48-FITC CD11B/C-BV510 CD45R-BV785 CD172-BV421 CD45-PE/Cy7 CD43-AF647 CD4-APC/Cy7 7AAD	CD32 CD3- FITC CD4-APC/Cy7 CD8-APC CD45R-BV785 7AAD
Tissues profiled	Brain, Bone marrow, Spleen and Blood	Cervical lymph nodes and Thymus

538 Flow cytometry data was acquired on an Fortessa X20 Cytometer (BD Biosciences, NJ, USA), and data
539 was analysed using FlowJo v10 Software (BD Life Sciences, NJ, USA). Live single cells were gated and
540 subsequent populations defined by the gating strategy illustrated in Figure S9.
541 *Histochemical staining and immunolocalisation*
542 Spleens, livers and kidneys were collected and washed in PBS before fixing in 4%PFA for 24 hours at
543 room temperature then processed and embedded into paraffin using routine methods. 4μM and
544 10μM sections were deparaffinised and rehydrated with standard methods; xylene followed by
545 descending ethanol series. 4μM sections were used for Sirius red and Hematoxylin and Eosin (H&E)
546 staining and 10μM sections for immunohistochemical staining as previously described (56, 110).
547 Briefly, sections were stained with Gill's No. 2 haematoxylin for 30 seconds and eosin for 40 seconds
548 for H&E staining and for Sirius red staining, sections were stained in Picric-Sirius Red solution

549 (Australian Biostain P/L, VIC, Australia) for 1hr. Heat-induced epitope retrieval was performed in 10
550 mM Sodium Citrate Buffer (pH6.0) followed by staining with rabbit anti-IBA1 (FUJIFILM, WAKO
551 chemicals, Richmond, Virginia, USA, 019-19741, 1:1000). 10mM EDTA buffer (pH 9.0) was used for
552 antigen retrieval for rabbit anti-CD163 (Abcam, ab182422, ERP19518, 1:500) and CD209B (Abcam,
553 ab308457,1:2000). Detection was performed with DAKO Envision Anti-rabbit HRP detection reagent
554 (Agilent). Sections were dehydrated in increasing ethanol series, cleared in xylene and coverslips
555 mounted with DPX mountant (Sigma). Whole slide digital scanning was performed on the VS120 or
556 VS200 at 40x objective magnification.
557 Free-floating sections of brain were generated and immunolocalisation of markers was performed as
558 described previously (66). For the older animals (>18 months), tissues were fixed by transcardial
559 perfusion with 4% paraformaldehyde in PBS and post fixed for 24hours at room temperature in
560 4%PFA/PBS. For analysis of young adult brains, sections were stained and imaged on Olympus FV3000
561 microscope as confocal images on either on the 40x or 60x oil objective with z stacks using solid state
562 lasers (405, 488 and 647 nm) for each brain region as follows:

Protein marker	**Antibody details**	**Cell identification**	**Objective used**	**Stacks**
IBA1	Wako Cat # 01-1874	Microglia	40× air	12
GFAP	Invitrogen Cat # PA1-10004	Astroglia	40× air	20
DCX	Cell signalling 4604s	Immature neurons	40× air and 60× oil	20 and 30
CD163	Abcam ab182422	Perivascular macrophages	40× air	12
TMEM119	Synaptic system 400-004	Microglia	20× air	20

563

564 For analysis of aged animals (>18 months) sections were stained and imaged on Olympus FV3000
565 microscope as confocal images on either on the 4x, 10x or 20x oil objective with z stacks using solid
566 state lasers (405, 488 and 647 nm) for each brain region as follows:

Protein marker	Antibody details	Cell identification	Objective used	Stacks
IBA1	Novachem Cat # 019-19741	Microglia	10x air	30
GFAP	Invitrogen Cat # PA1-10004	Astroglia	4x air	40
WFA	VectorLabs Cat # ZH0824	Perineuronal nets	20x air	30
PV	Synaptic Systems Cat # 195004	Parvalbumin neurons	20x air	30
Risedronate	BioVinc LLC Cat # BV500101	Fluorescent bisphosphonate analogue	4x air	40

567

568 *Image analysis*

569 Images were taken as a z-stack of 1 µm thickness and converted to Z-project on Image J with FIJI
570 software (version 1.54f). A minimum of 4 images per brain section were analysed for either number
571 of positive cells (IBA1, PV) or percentage area (GFAP, WFA) as follows: Images were Z-projected and
572 converted to RGB image and colour thresholding was performed using either default method (Iba1,
573 GFAP) or MaxEntropy method (WFA, PV) with the same settings across genotypes. Raw data was
574 collected using the measure tool and values were plotted on GraphPad Prism (version 10.3.1).

575 *Diffusion Tensor imaging and analysis*

576 Fixed brains were washed in 0.1 M PBS for >1 week for scanning using a 16.4 T vertical bore MR
577 microimaging system (Bruker Biospin, rheinstetten, Germany; Paravision v6.01), equipped with a
578 Micro2.5 imaging gradient using a 20 mm linear surface acoustic wave coil (M2M, Brisbane, Australia).
579 3D T1/T2*-weighted multi gradient echo (MGE) images were acquired with TR = 70 ms, bandwidth =
580 100 KHz, FOV = 27 × 18 × 15 mm and matrix size = 216 × 144 × 120, resulting in 120 µm 3D isotropic
581 image resolution, with the acquisition time of 40 mins. The MGE data contained fifteen TEs (= 4, 8,12,
582 ... 60 ms) for Quantitative Susceptibility Mapping. Subsequently, samples were washed in 0.1 M PBS
583 with 0.2% v/v Magnevist (Bayer) for >1 week. 3D DWI data were acquired using a Stejskal-Tanner DWI
584 spin-echo sequence with TR = 200 ms, TE = 21 ms, δ/Δ = 2.5/12 ms, bandwidth = 50 KHz, FOV = 27 ×
585 18 × 15 mm and matrix size = 180 × 120 × 100, image resolution = 150 µm, 30 direction diffusion
586 encoding with b-value = 5000 s/mm2, three b = 0 images, with the acquisition time of 15 h 42 min.
587 Quantitative susceptibility maps (QSM) and T2* relaxation maps of the rat brains were calculated
588 using the program (QSMxT) (111). The anatomical images were constructed by combining multi-echo
589 images to enhance image contrast. Images were registered into the Waxholm Space MRI/DTI template
590 for the Sprague Dawley rat brain**,** using ANTs diffeomorphic image registration (112-114). The model-
591 based segmentation of brain regions was performed on each sample and their image volumes and
592 intensities were measured using ITK-SNAP.
593 The FID of DWI datasets were zero-filled by a factor of 1.5 in all dimensions prior to Fourier transform
594 to improve fibre tracking. DWI data were bias corrected using ANTs N4BiasFieldCorrection and
595 processed using MRtrix3 software (www.mrtrix.org). Fiber orientation distribution (FOD) was
596 reconstructed using constrained spherical deconvolution (CSD) method, and probabilistic
597 tractography was performed using iFOD2 algorithm. Tractography was performed for specific major
598 white matter (WM) tracts. Firstly, the seeding regions of interest (ROIs) were manually drawn in the
599 midsagittal and coronal sections of the colour vector map, and fibretracks were generated for the
600 corpus callosum (CC), hippocampal commissure (HC), internal capsule (IC) and anterior commissure

601 (AC) at 100 seeds per voxel. The volumes of the white matter tracts were measured from Tract Density
602 Intensity maps (TDI) with the intensity threshold set at 20% to remove background noise from
603 probabilistic tracking (112, 115).

604 *PET/MR imaging of DPA714 uptake*

605 DPA714-F18 was synthesized as previously described (78). Anesthesized rats, with a cannulated tail
606 vein (with a 0.020" ×0.060" OD Tygon microbore tubing, 45 cm long and a 25 gauge needle) were
607 placed in a combined MRI/PET system, comprising a Bruker AV4 70/30 BioSpec MRI including a 7T,
608 300 mm bore magnet with B-GA20S HP gradients and operating with Paravision 360 V3.5. The PET
609 images are acquired on a 3-ring PET insert with an axial FOV of 150mm, transaxial FOV of 80 mm. A
610 40 mm ID rat head MRI rf coil inside the PET ring was used to acquire head images simultaneously
611 with the PET acquisition. A 60 min PET and dynamic GE images with 200 repetitions were started
612 simultaneously. After approximately 2 min of scanning the rats were injected with approximately 30
613 MBq of PET tracer solution, 300 µl Gadovist and saline/10% ethanol to give a total volume of 400µl.
614 This volume was injected manually via the catheter inserted into the tail vein in a slow bolus injection.
615 Following 12 min of dynamic GE scanning, the following MR scanning was performed during the PET
616 acquisition:

617 PET reconstruction was performed using OSEM 0.5 with iterations = 1, Scatter correction, Randoms
618 correction, Decay correction, Partial volume correction, point spread function correction, attenuation
619 correction generated from the 3D FISP 250 µm coronal sequence and partitioning of 10 x 60 sec and
620 10 x 300 sec time frames. The dynamic PET series were then geometrically registered to the T2
621 turboRARE transverse image set and the 3D FISP 250 µm image set. PET/MR data were analysed using
622 the PMOD software. PET and MR data for each animal were matched, registered onto the Schiffer rat
623 brain atlas and segmented (116). SUV/BW values were calculated after normalizing for decay and
624 bodyweight of each animal scanned.

625 *Molecular profiling and RNAseq of brain regions and Kidney*

626 Brain tissue from one hemisphere was minced and snap frozen. RNA was extracted using TRIzol
627 reagent using standard manufacturer's protocol. 1μg of RNA was used to synthesize cDNA according
628 to manufacturer's protocol (Meridian bioscience). qRT-PCR was performed with 2x SYBR green
629 reagent (Thermofisher) with the primer sequences (56). Cortex, hippocampus, and thalamus were
630 sampled using a biopsy punch (1mm diameter) and placed directly into TRIzol and RNA extracted.
631 Whole kidneys were snap frozen at collection and RNA extracted using TRIzol reagent.

632 Library preparation and sequencing was performed at the University of Queensland Sequencing
633 Facility (University of Queensland, Brisbane, Australia). Bar-coded RNA-Sequencing (RNA-Seq)
634 libraries were generated using the Illumina Stranded mRNA Library Prep Ligation kit (Illumina, CA,
635 USA) and IDT for Illumina RNA UD Indexes (Illumina, CA, USA). The bar coded RNA libraries were
636 pooled in equimolar ratios prior to sequencing using the Illumina NovaSeq 6000 (Illumina, CA, USA).
637 Paired-end 102 bp reads were generated using either a NovaSeq S2 reagent kit v1.5 (200 cycles)
638 (Illumina, CA, USA). After sequencing, fastq files were created using bcl2fastq2 (v2.20.0.422). Raw
639 sequencing data (in the form of .fastq files) was provided by the sequencing facility for further analysis.
640 Raw reads were pre-processed using fastp v0.23.2 using previously described parameters (52, 117)
641 FastQC was used on pre and post-trimmed reads to ensure adequate sequence quality, GC content,
642 and removal of adapter sequences (118).

643 The reference transcriptome used in this study was created by combining the unique protein-coding
644 transcripts from the Ensembl and NCBI RefSeq databases of the Rnor6.0 annotation, as previously
645 described (55). After pre-processing, transcript expression level was quantified as transcripts per
646 million using Kallisto (v0.46.0).(119) Kallisto expression files were imported into RStudio (R version
647 4.2.1) using the tximport package (v1.24.0) to collate transcript-level TPM generated by Kallisto into
648 gene-level TPMs for use by downstream tools.

649 All network cluster analysis was based on gene-level expression and was conducted using Graphia
650 (https://graphia.app) (120). Only genes expressed at ≥ 1 TPM in at least 2 samples were retained for

651 analysis. A network graph was then created where nodes (genes) were connected by edges
652 (representing correlation coefficients). Relationships where $r \geq 0.85$ were included. Samples which
653 exhibited similar patterns of gene expression across tissues were placed close together in the network
654 graph. Gene expression patterns were further characterised using the Markov Cluster Algorithm (MCL)
655 with an inflation value of 2.0 to identify clusters of transcripts with similar expression patterns.

656 *Statistics*

657 All data are presented as mean ± standard deviation and analysed with Graphpad Prism (9.0 or 10.0).
658 Statistical testing was performed using an ANOVA with Tukey post-hoc analysis or t-test for pairwise
659 comparisons. P values <0.05 are considered significant.

660 *Data availability*

661 All data are provided in supplemental file. Sequencing data can be accessed through accession number
662

663 References

664 1. Cox N, Pokrovskii M, Vicario R, and Geissmann F. Origins, Biology, and Diseases of Tissue
665 Macrophages. *Annu Rev Immunol.* 2021;39:313-44.
666 2. Hume DA, Irvine KM, and Pridans C. The Mononuclear Phagocyte System: The Relationship
667 between Monocytes and Macrophages. *Trends Immunol.* 2019;40(2):98-112.
668 3. Jenkins SJ, and Allen JE. The expanding world of tissue-resident macrophages. *Eur J Immunol.*
669 2021;51(8):1882-96.
670 4. Lazarov T, Juarez-Carreno S, Cox N, and Geissmann F. Physiology and diseases of tissue-
671 resident macrophages. *Nature.* 2023;618(7966):698-707.
672 5. Mass E, Nimmerjahn F, Kierdorf K, and Schlitzer A. Tissue-specific macrophages: how they
673 develop and choreograph tissue biology. *Nat Rev Immunol.* 2023;23(9):563-79.
674 6. Grabert K, Sehgal A, Irvine KM, Wollscheid-Lengeling E, Ozdemir DD, Stables J, et al. A
675 Transgenic Line That Reports CSF1R Protein Expression Provides a Definitive Marker for the
676 Mouse Mononuclear Phagocyte System. *J Immunol.* 2020;205(11):3154-66.
677 7. Chitu V, and Stanley ER. Regulation of Embryonic and Postnatal Development by the CSF-1
678 Receptor. *Curr Top Dev Biol.* 2017;123:229-75.
679 8. Hume DA, Caruso M, Ferrari-Cestari M, Summers KM, Pridans C, and Irvine KM. Phenotypic
680 impacts of CSF1R deficiencies in humans and model organisms. *J Leukoc Biol.*
681 2020;107(2):205-19.
682 9. MacDonald KP, Palmer JS, Cronau S, Seppanen E, Olver S, Raffelt NC, et al. An antibody
683 against the colony-stimulating factor 1 receptor depletes the resident subset of monocytes
684 and tissue- and tumor-associated macrophages but does not inhibit inflammation. *Blood.*
685 2010;116(19):3955-63.
686 10. Cecchini MG, Dominguez MG, Mocci S, Wetterwald A, Felix R, Fleisch H, et al. Role of colony
687 stimulating factor-1 in the establishment and regulation of tissue macrophages during
688 postnatal development of the mouse. *Development.* 1994;120(6):1357-72.
689 11. Van Wesenbeeck L, Odgren PR, MacKay CA, D'Angelo M, Safadi FF, Popoff SN, et al. The
690 osteopetrotic mutation toothless (tl) is a loss-of-function frameshift mutation in the rat Csf1
691 gene: Evidence of a crucial role for CSF-1 in osteoclastogenesis and endochondral
692 ossification. *Proc Natl Acad Sci U S A.* 2002;99(22):14303-8.
693 12. Dai XM, Ryan GR, Hapel AJ, Dominguez MG, Russell RG, Kapp S, et al. Targeted disruption of
694 the mouse colony-stimulating factor 1 receptor gene results in osteopetrosis, mononuclear
695 phagocyte deficiency, increased primitive progenitor cell frequencies, and reproductive
696 defects. *Blood.* 2002;99(1):111-20.
697 13. Lin H, Lee E, Hestir K, Leo C, Huang M, Bosch E, et al. Discovery of a cytokine and its receptor
698 by functional screening of the extracellular proteome. *Science.* 2008;320(5877):807-11.
699 14. Garceau V, Smith J, Paton IR, Davey M, Fares MA, Sester DP, et al. Pivotal Advance: Avian
700 colony-stimulating factor 1 (CSF-1), interleukin-34 (IL-34), and CSF-1 receptor genes and
701 gene products. *J Leukoc Biol.* 2010;87(5):753-64.
702 15. Hume DA, Gutowska-Ding MW, Garcia-Morales C, Kebede A, Bamidele O, Trujillo AV, et al.
703 Functional evolution of the colony-stimulating factor 1 receptor (CSF1R) and its ligands in
704 birds. *J Leukoc Biol.* 2020;107(2):237-50.
705 16. Kuil LE, Oosterhof N, Geurts SN, van der Linde HC, Meijering E, and van Ham TJ. Reverse
706 genetic screen reveals that Il34 facilitates yolk sac macrophage distribution and seeding of
707 the brain. *Dis Model Mech.* 2019;12(3):dmm037762.
708 17. Wang T, Kono T, Monte MM, Kuse H, Costa MM, Korenaga H, et al. Identification of IL-34 in
709 teleost fish: differential expression of rainbow trout IL-34, MCSF1 and MCSF2, ligands of the
710 MCSF receptor. *Mol Immunol.* 2013;53(4):398-409.
711 18. Wu S, Xue R, Hassan S, Nguyen TML, Wang T, Pan H, et al. Il34-Csf1r Pathway Regulates the
712 Migration and Colonization of Microglial Precursors. *Dev Cell.* 2018;46(5):552-63 e4.

713 19. Yu T, Kuang H, Wu X, Huang Y, Wang J, and Wen Z. Cell competition for neuron-derived
714 trophic factor controls the turnover and lifespan of microglia. *Sci Adv.* 2023;9(24):eadf9790.
715 20. Ma X, Lin WY, Chen Y, Stawicki S, Mukhyala K, Wu Y, et al. Structural basis for the dual
716 recognition of helical cytokines IL-34 and CSF-1 by CSF-1R. *Structure.* 2012;20(4):676-87.
717 21. Lelios I, Cansever D, Utz SG, Mildenberger W, Stifter SA, and Greter M. Emerging roles of IL-
718 34 in health and disease. *J Exp Med.* 2020;217(3):e20190290.
719 22. Wei S, Nandi S, Chitu V, Yeung YG, Yu W, Huang M, et al. Functional overlap but differential
720 expression of CSF-1 and IL-34 in their CSF-1 receptor-mediated regulation of myeloid cells. *J*
721 *Leukoc Biol.* 2010;88(3):495-505.
722 23. Greter M, Lelios I, Pelczar P, Hoeffel G, Price J, Leboeuf M, et al. Stroma-derived interleukin-
723 34 controls the development and maintenance of langerhans cells and the maintenance of
724 microglia. *Immunity.* 2012;37(6):1050-60.
725 24. Wang Y, Szretter KJ, Vermi W, Gilfillan S, Rossini C, Cella M, et al. IL-34 is a tissue-restricted
726 ligand of CSF1R required for the development of Langerhans cells and microglia. *Nat*
727 *Immunol.* 2012;13(8):753-60.
728 25. Nandi S, Gokhan S, Dai XM, Wei S, Enikolopov G, Lin H, et al. The CSF-1 receptor ligands IL-34
729 and CSF-1 exhibit distinct developmental brain expression patterns and regulate neural
730 progenitor cell maintenance and maturation. *Dev Biol.* 2012;367(2):100-13.
731 26. Easley-Neal C, Foreman O, Sharma N, Zarrin AA, and Weimer RM. CSF1R Ligands IL-34 and
732 CSF1 Are Differentially Required for Microglia Development and Maintenance in White and
733 Gray Matter Brain Regions. *Front Immunol.* 2019;10:2199.
734 27. Kana V, Desland FA, Casanova-Acebes M, Ayata P, Badimon A, Nabel E, et al. CSF-1 controls
735 cerebellar microglia and is required for motor function and social interaction. *J Exp Med.*
736 2019;216(10):2265-81.
737 28. Nandi S, Cioce M, Yeung YG, Nieves E, Tesfa L, Lin H, et al. Receptor-type protein-tyrosine
738 phosphatase zeta is a functional receptor for interleukin-34. *J Biol Chem.*
739 2013;288(30):21972-86.
740 29. Segaliny AI, Brion R, Mortier E, Maillasson M, Cherel M, Jacques Y, et al. Syndecan-1
741 regulates the biological activities of interleukin-34. *Biochim Biophys Acta.*
742 2015;1853(5):1010-21.
743 30. Xie X, Zhang W, Xiao M, Wei T, Qiu Y, Qiu J, et al. TREM2 acts as a receptor for IL-34 to
744 suppress acute myeloid leukemia in mice. *Blood.* 2023;141(26):3184-98.
745 31. Abdel-Rehim AS, Mohamed NA, and Shakweer MM. Interleukin-34 as a marker for
746 subclinical proliferative lupus nephritis. *Lupus.* 2020;29(6):607-16.
747 32. Baghdadi M, Umeyama Y, Hama N, Kobayashi T, Han N, Wada H, and Seino KI. Interleukin-
748 34, a comprehensive review. *J Leukoc Biol.* 2018;104(5):931-51.
749 33. Franze E, Laudisi F, Di Grazia A, Maronek M, Bellato V, Sica G, and Monteleone G.
750 Macrophages produce and functionally respond to interleukin-34 in colon cancer. *Cell Death*
751 *Discov.* 2020;6(1):117.
752 34. Franze E, Monteleone I, Cupi ML, Mancia P, Caprioli F, Marafini I, et al. Interleukin-34
753 sustains inflammatory pathways in the gut. *Clin Sci (Lond).* 2015;129(3):271-80.
754 35. Franze E, Stolfi C, Troncone E, Scarozza P, and Monteleone G. Role of Interleukin-34 in
755 Cancer. *Cancers (Basel).* 2020;12(1):252.
756 36. Kashiwagi M, Ozaki Y, Imanishi T, Taruya A, Kuroi A, Katayama Y, et al. Interleukin-34 levels
757 are increased in acute myocardial infarction and associated with major adverse
758 cardiovascular events. *Coron Artery Dis.* 2022;31(1):61-3.
759 37. Liu Y, Zhang B, Lei Y, Xia L, Lu J, and Shen H. Serum levels of interleukin-34 and clinical
760 correlation in patients with primary Sjogren's syndrome. *Int J Rheum Dis.* 2020;23(3):374-80.
761 38. Masteller EL, and Wong BR. Targeting IL-34 in chronic inflammation. *Drug Discov Today.*
762 2014;19(8):1212-6.

763 39. Munoz-Garcia J, Cochonneau D, Teletchea S, Moranton E, Lanoe D, Brion R, et al. The twin
764 cytokines interleukin-34 and CSF-1: masterful conductors of macrophage homeostasis.
765 *Theranostics.* 2021;11(4):1568-93.
766 40. Nakamichi Y, Udagawa N, and Takahashi N. IL-34 and CSF-1: similarities and differences. *J*
767 *Bone Miner Metab.* 2013;31(5):486-95.
768 41. Otsuka R, Wada H, and Seino KI. IL-34, the rationale for its expression in physiological and
769 pathological conditions. *Semin Immunol.* 2021;54:101517.
770 42. Shang J, Xu Y, Pu S, Sun X, and Gao X. Role of IL-34 and its receptors in inflammatory
771 diseases. *Cytokine.* 2023;171:156348.
772 43. Zwicker S, Martinez GL, Bosma M, Gerling M, Clark R, Majster M, et al. Interleukin 34: a new
773 modulator of human and experimental inflammatory bowel disease. *Clin Sci (Lond).*
774 2015;129(3):281-90.
775 44. Bezie S, Freuchet A, Serazin C, Salama A, Vimond N, Anegon I, and Guillonneau C. IL-34
776 Actions on FOXP3(+) Tregs and CD14(+) Monocytes Control Human Graft Rejection. *Front*
777 *Immunol.* 2020;11:1496.
778 45. Bezie S, Picarda E, Ossart J, Tesson L, Usal C, Renaudin K, et al. IL-34 is a Treg-specific
779 cytokine and mediates transplant tolerance. *J Clin Invest.* 2015;125(10):3952-64.
780 46. Baek JH, Zeng R, Weinmann-Menke J, Valerius MT, Wada Y, Ajay AK, et al. IL-34 mediates
781 acute kidney injury and worsens subsequent chronic kidney disease. *J Clin Invest.*
782 2015;125(8):3198-214.
783 47. Wada Y, Gonzalez-Sanchez HM, Weinmann-Menke J, Iwata Y, Ajay AK, Meineck M, and
784 Kelley VR. IL-34-Dependent Intrarenal and Systemic Mechanisms Promote Lupus Nephritis in
785 MRL-Fas(lpr) Mice. *J Am Soc Nephrol.* 2019;30(2):244-59.
786 48. Isbel NM, Hill PA, Foti R, Mu W, Hurst LA, Stambe C, et al. Tubules are the major site of M-
787 CSF production in experimental kidney disease: correlation with local macrophage
788 proliferation. *Kidney Int.* 2001;60(2):614-25.
789 49. Le Meur Y, Tesch GH, Hill PA, Mu W, Foti R, Nikolic-Paterson DJ, and Atkins RC. Macrophage
790 accumulation at a site of renal inflammation is dependent on the M-CSF/c-fms pathway. *J*
791 *Leukoc Biol.* 2002;72(3):530-7.
792 50. Alikhan MA, Jones CV, Williams TM, Beckhouse AG, Fletcher AL, Kett MM, et al. Colony-
793 stimulating factor-1 promotes kidney growth and repair via alteration of macrophage
794 responses. *Am J Pathol.* 2011;179(3):1243-56.
795 51. Hume DA, Caruso M, Keshvari S, Patkar OL, Sehgal A, Bush SJ, et al. The Mononuclear
796 Phagocyte System of the Rat. *J Immunol.* 2021;206(10):2251-63.
797 52. Keshvari S, Caruso M, Teakle N, Batoon L, Sehgal A, Patkar OL, et al. CSF1R-dependent
798 macrophages control postnatal somatic growth and organ maturation. *PLoS Genet.*
799 2021;17(6):e1009605.
800 53. Pridans C, Raper A, Davis GM, Alves J, Sauter KA, Lefevre L, et al. Pleiotropic Impacts of
801 Macrophage and Microglial Deficiency on Development in Rats with Targeted Mutation of
802 the Csf1r Locus. *J Immunol.* 2018;201(9):2683-99.
803 54. Consortium F, the RP, Clst, Forrest AR, Kawaji H, Rehli M, et al. A promoter-level mammalian
804 expression atlas. *Nature.* 2014;507(7493):462-70.
805 55. Summers KM, Bush SJ, Wu C, and Hume DA. Generation and network analysis of an RNA-seq
806 transcriptional atlas for the rat. *NAR Genom Bioinform.* 2022;4(1):lqac017.
807 56. Carter-Cusack D, Huang S, Keshvari S, Patkar O, Sehgal A, Allavena R, et al. Wild-type bone
808 marrow cells repopulate tissue resident macrophages and reverse the impacts of
809 homozygous CSF1R mutation. *PLoS Genetics.* 2024:In press.
810 57. Freuchet A, Salama A, Bezie S, Tesson L, Remy S, Humeau R, et al. IL-34 deficiency impairs
811 FOXP3(+) Treg function in a model of autoimmune colitis and decreases immune tolerance
812 homeostasis. *Clin Transl Med.* 2022;12(8):e988.

58. Irvine KM, Caruso M, Cestari MF, Davis GM, Keshvari S, Sehgal A, et al. Analysis of the impact of CSF-1 administration in adult rats using a novel Csf1r-mApple reporter gene. *J Leukoc Biol.* 2020;107(2):221-35.
59. Sehgal A, Carter-Cusack D, Keshvari S, Patkar O, Huang S, Summers KM, et al. Intraperitoneal transfer of wild-type bone marrow repopulates tissue macrophages in the Csf1r knockout rat without contributing to monocytopoiesis. *Eur J Immunol.* 2023;53(8):e2250312.
60. Wang Y, and Colonna M. Interkeukin-34, a cytokine crucial for the differentiation and maintenance of tissue resident macrophages and Langerhans cells. *Eur J Immunol.* 2014;44(6):1575-81.
61. Gu X, Heinrich A, Li SY, and DeFalco T. Testicular macrophages are recruited during a narrow fetal time window and promote organ-specific developmental functions. *Nat Commun.* 2023;14(1):1439.
62. Mossadegh-Keller N, Gentek R, Gimenez G, Bigot S, Mailfert S, and Sieweke MH. Developmental origin and maintenance of distinct testicular macrophage populations. *J Exp Med.* 2017;214(10):2829-41.
63. Mossadegh-Keller N, and Sieweke MH. Characterization of Mouse Adult Testicular Macrophage Populations by Immunofluorescence Imaging and Flow Cytometry. *Bio Protoc.* 2019;9(5):e3178.
64. Paolicelli RC, Sierra A, Stevens B, Tremblay ME, Aguzzi A, Ajami B, et al. Microglia states and nomenclature: A field at its crossroads. *Neuron.* 2022;110(21):3458-83.
65. Zhang Z, Zhang ZY, Wu Y, and Schluesener HJ. Lesional accumulation of CD163+ macrophages/microglia in rat traumatic brain injury. *Brain Res.* 2012;1461:102-10.
66. Patkar OL, Caruso M, Teakle N, Keshvari S, Bush SJ, Pridans C, et al. Analysis of homozygous and heterozygous Csf1r knockout in the rat as a model for understanding microglial function in brain development and the impacts of human CSF1R mutations. *Neurobiol Dis.* 2021;151:105268.
67. Devlin BA, Nguyen DM, Grullon G, Clark MJ, Ceasrine AM, Deja M, et al. Neuron Derived Cytokine Interleukin-34 Controls Developmental Microglia Function. *bioRxiv.* 2024;2024:2024.05.10.589920.
68. Buttgereit A, Lelios I, Yu X, Vrohlings M, Krakoski NR, Gautier EL, et al. Sall1 is a transcriptional regulator defining microglia identity and function. *Nat Immunol.* 2016;17(12):1397-406.
69. Fixsen BR, Han CZ, Zhou Y, Spann NJ, Saisan P, Shen Z, et al. SALL1 enforces microglia-specific DNA binding and function of SMADs to establish microglia identity. *Nat Immunol.* 2023;24(7):1188-99.
70. Dulski J, Muthusamy K, Lund TC, and Wszolek ZK. CSF1R-related disorder: State of the art, challenges, and proposition of a new terminology. *Parkinsonism Relat Disord.* 2024;121:105894.
71. Ellenbroek B, and Youn J. Rodent models in neuroscience research: is it a rat race? *Dis Model Mech.* 2016;9(10):1079-87.
72. Bradford BM, McGuire LI, Hume DA, Pridans C, and Mabbott NA. Microglia deficiency accelerates prion disease but does not enhance prion accumulation in the brain. *Glia.* 2022;70(11):2169-87.
73. Kiani Shabestari S, Morabito S, Danhash EP, McQuade A, Sanchez JR, Miyoshi E, et al. Absence of microglia promotes diverse pathologies and early lethality in Alzheimer's disease mice. *Cell Rep.* 2022;39(11):110961.
74. Vicidomini C, Panico M, Greco A, Gargiulo S, Coda AR, Zannetti A, et al. In vivo imaging and characterization of [(18)F]DPA-714, a potential new TSPO ligand, in mouse brain and peripheral tissues using small-animal PET. *Nucl Med Biol.* 2015;42(3):309-16.

75. Alam MM, Lee J, and Lee SY. Recent Progress in the Development of TSPO PET Ligands for Neuroinflammation Imaging in Neurological Diseases. *Nucl Med Mol Imaging.* 2017;51(4):283-96.
76. Crawshaw AA, and Robertson NP. The role of TSPO PET in assessing neuroinflammation. *J Neurol.* 2017;264(8):1825-7.
77. Guilarte TR, Rodichkin AN, McGlothan JL, Acanda De La Rocha AM, and Azzam DJ. Imaging neuroinflammation with TSPO: A new perspective on the cellular sources and subcellular localization. *Pharmacol Ther.* 2022;234:108048.
78. James ML, Fulton RR, Vercoullie J, Henderson DJ, Garreau L, Chalon S, et al. DPA-714, a new translocator protein-specific ligand: synthesis, radiofluorination, and pharmacologic characterization. *J Nucl Med.* 2008;49(5):814-22.
79. Golla SS, Boellaard R, Oikonen V, Hoffmann A, van Berckel BN, Windhorst AD, et al. Quantification of [18F]DPA-714 binding in the human brain: initial studies in healthy controls and Alzheimer's disease patients. *J Cereb Blood Flow Metab.* 2015;35(5):766-72.
80. Peyronneau MA, Kuhnast B, Nguyen DL, Jego B, Sayet G, Caille F, et al. [(18)F]DPA-714: Effect of co-medications, age, sex, BMI and TSPO polymorphism on the human plasma input function. *Eur J Nucl Med Mol Imaging.* 2023;50(11):3251-64.
81. Arreola MA, Soni N, Crapser JD, Hohsfield LA, Elmore MRP, Matheos DP, et al. Microglial dyshomeostasis drives perineuronal net and synaptic loss in a CSF1R(+/-) mouse model of ALSP, which can be rescued via CSF1R inhibitors. *Sci Adv.* 2021;7(35):eabg1601.
82. Crapser JD, Spangenberg EE, Barahona RA, Arreola MA, Hohsfield LA, and Green KN. Microglia facilitate loss of perineuronal nets in the Alzheimer's disease brain. *EBioMedicine.* 2020;58:102919.
83. Chadarevian JP, Hasselmann J, Lahian A, Capocchi JK, Escobar A, Lim TE, et al. Therapeutic potential of human microglia transplantation in a chimeric model of CSF1R-related leukoencephalopathy. *Neuron.* 2024;112(16):2686-707 e8.
84. Munro DAD, Bestard-Cuche N, McQuade A, Chagnot A, Kiani Shabestari S, Chadarevian JP, et al. Microglia provide resilience against region-selective neuropathology with ageing. *Neuron.* 2024;In press.
85. Diwan V, Brown L, and Gobe GC. Adenine-induced chronic kidney disease in rats. *Nephrology (Carlton).* 2018;23(1):5-11.
86. Diwan V, Small D, Kauter K, Gobe GC, and Brown L. Gender differences in adenine-induced chronic kidney disease and cardiovascular complications in rats. *Am J Physiol Renal Physiol.* 2014;307(11):F1169-78.
87. Cantero-Navarro E, Rayego-Mateos S, Orejudo M, Tejedor-Santamaria L, Tejera-Munoz A, Sanz AB, et al. Role of Macrophages and Related Cytokines in Kidney Disease. *Front Med (Lausanne).* 2021;8:688060.
88. Giotti B, Chen SH, Barnett MW, Regan T, Ly T, Wiemann S, et al. Assembly of a parts list of the human mitotic cell cycle machinery. *J Mol Cell Biol.* 2019;11(8):703-18.
89. Summers KM, Bush SJ, and Hume DA. Network analysis of transcriptomic diversity amongst resident tissue macrophages and dendritic cells in the mouse mononuclear phagocyte system. *PLoS Biol.* 2020;18(10):e3000859.
90. Djudjaj S, Papasotiriou M, Bulow RD, Wagnerova A, Lindenmeyer MT, Cohen CD, et al. Keratins are novel markers of renal epithelial cell injury. *Kidney Int.* 2016;89(4):792-808.
91. Wozniak J, Floege J, Ostendorf T, and Ludwig A. Key metalloproteinase-mediated pathways in the kidney. *Nat Rev Nephrol.* 2021;17(8):513-27.
92. Pap D, Veres-Szekely A, Szebeni B, Rokonay R, Onody A, Lippai R, et al. Characterization of IL-19, -20, and -24 in acute and chronic kidney diseases reveals a pro-fibrotic role of IL-24. *J Transl Med.* 2020;18(1):172.

911 93. Schutte-Nutgen K, Edeling M, Kentrup D, Heitplatz B, Van Marck V, Zarbock A, et al.
912 Interleukin 24 promotes cell death in renal epithelial cells and is associated with acute renal
913 injury. *Am J Transplant.* 2022;22(11):2548-59.
914 94. Ludwig-Portugall I, Bartok E, Dhana E, Evers BD, Primiano MJ, Hall JP, et al. An NLRP3-specific
915 inflammasome inhibitor attenuates crystal-induced kidney fibrosis in mice. *Kidney Int.*
916 2016;90(3):525-39.
917 95. Bhairavabhotla R, Kim YC, Glass DD, Escobar TM, Patel MC, Zahr R, et al. Transcriptome
918 profiling of human FoxP3+ regulatory T cells. *Hum Immunol.* 2016;77(2):201-13.
919 96. Luo Y, Xu C, Wang B, Niu Q, Su X, Bai Y, et al. Single-cell transcriptomic analysis reveals
920 disparate effector differentiation pathways in human T(reg) compartment. *Nat Commun.*
921 2021;12(1):3913.
922 97. Menoret S, Tesson L, Remy S, Gourain V, Serazin C, Usal C, et al. CD4(+) and CD8(+)
923 regulatory T cell characterization in the rat using a unique transgenic Foxp3-EGFP model.
924 *BMC Biol.* 2023;21(1):8.
925 98. Lawson LJ, Perry VH, Dri P, and Gordon S. Heterogeneity in the distribution and morphology
926 of microglia in the normal adult mouse brain. *Neuroscience.* 1990;39(1):151-70.
927 99. Askew K, Li K, Olmos-Alonso A, Garcia-Moreno F, Liang Y, Richardson P, et al. Coupled
928 Proliferation and Apoptosis Maintain the Rapid Turnover of Microglia in the Adult Brain. *Cell*
929 *Rep.* 2017;18(2):391-405.
930 100. Stables J, Green EK, Sehgal A, Patkar OL, Keshvari S, Taylor I, et al. A kinase-dead Csf1r
931 mutation associated with adult-onset leukoencephalopathy has a dominant inhibitory
932 impact on CSF1R signalling. *Development.* 2022;149(8):dev200237.
933 101. Sehgal A, Irvine KM, and Hume DA. Functions of macrophage colony-stimulating factor
934 (CSF1) in development, homeostasis, and tissue repair. *Semin Immunol.* 2021;54:101509.
935 102. McNamara NB, Munro DAD, Bestard-Cuche N, Uyeda A, Bogie JFJ, Hoffmann A, et al.
936 Microglia regulate central nervous system myelin growth and integrity. *Nature.*
937 2023;613(7942):120-9.
938 103. Liu YJ, Spangenberg EE, Tang B, Holmes TC, Green KN, and Xu X. Microglia Elimination
939 Increases Neural Circuit Connectivity and Activity in Adult Mouse Cortex. *J Neurosci.*
940 2021;41(6):1274-87.
941 104. O'Keeffe M, Sam Booker, Darren Walsh, Mosi Li, Chloe Henley, Laura Simoes de Oliveira, et
942 al. Typical development of synaptic and neuronal properties can proceed without microglia.
943 *Biorxiv.* 2024:2024.09. 06.611614.
944 105. Berglund R, Cheng Y, Piket E, M ZA, Zeitelhofer M, Olsson T, et al. The aging mouse CNS is
945 protected by an autophagy-dependent microglia population promoted by IL-34. *Nat*
946 *Commun.* 2024;15(1):383.
947 106. de Rojas I, Moreno-Grau S, Tesi N, Grenier-Boley B, Andrade V, Jansen IE, et al. Common
948 variants in Alzheimer's disease and risk stratification by polygenic risk scores. *Nat Commun.*
949 2021;12(1):3417.
950 107. Rogers NM, Ferenbach DA, Isenberg JS, Thomson AW, and Hughes J. Dendritic cells and
951 macrophages in the kidney: a spectrum of good and evil. *Nat Rev Nephrol.* 2014;10(11):625-
952 43.
953 108. Liu ZX, Chen WJ, Wang Y, Chen BQ, Liu YC, Cheng TC, et al. Interleukin-34 deficiency
954 aggravates development of colitis and colitis-associated cancer in mice. *World J*
955 *Gastroenterol.* 2022;28(47):6752-68.
956 109. Batoon L, Keshvari S, Irvine KM, Ho E, Caruso M, Patkar OL, et al. Relative contributions of
957 osteal macrophages and osteoclasts to postnatal bone development in CSF1R-deficient rats
958 and phenotype rescue following wild-type bone marrow cell transfer. *J Leukoc Biol.* 2024.
959 110. Huang S, Carter-Cusack D, Maxwell E, Patkar OL, Irvine KM, and Hume DA. Genetic and
960 Immunohistochemistry Tools to Visualize Rat Macrophages In Situ. *Methods Mol Biol.*
961 2024;2713:99-115.

111. Stewart AW, Robinson SD, O'Brien K, Jin J, Widhalm G, Hangel G, et al. QSMxT: Robust masking and artifact reduction for quantitative susceptibility mapping. *Magn Reson Med.* 2022;87(3):1289-300.
112. Avants BB, Tustison NJ, Song G, Cook PA, Klein A, and Gee JC. A reproducible evaluation of ANTs similarity metric performance in brain image registration. *Neuroimage.* 2011;54(3):2033-44.
113. Johnson GA, Calabrese E, Badea A, Paxinos G, and Watson C. A multidimensional magnetic resonance histology atlas of the Wistar rat brain. *Neuroimage.* 2012;62(3):1848-56.
114. Papp EA, Leergaard TB, Calabrese E, Johnson GA, and Bjaalie JG. Waxholm Space atlas of the Sprague Dawley rat brain. *Neuroimage.* 2014;97:374-86.
115. Calamante F, Tournier JD, Kurniawan ND, Yang Z, Gyengesi E, Galloway GJ, et al. Super-resolution track-density imaging studies of mouse brain: comparison to histology. *Neuroimage.* 2012;59(1):286-96.
116. Schiffer WK, Mirrione MM, Biegon A, Alexoff DL, Patel V, and Dewey SL. Serial microPET measures of the metabolic reaction to a microdialysis probe implant. *J Neurosci Methods.* 2006;155(2):272-84.
117. Chen S, Zhou Y, Chen Y, and Gu J. fastp: an ultra-fast all-in-one FASTQ preprocessor. *Bioinformatics.* 2018;34(17):i884-i90.
118. Wingett SW, and Andrews S. FastQ Screen: A tool for multi-genome mapping and quality control. *F1000Res.* 2018;7:1338.
119. Bray NL, Pimentel H, Melsted P, and Pachter L. Near-optimal probabilistic RNA-seq quantification. *Nat Biotechnol.* 2016;34(5):525-7.
120. Freeman TC, Horsewell S, Patir A, Harling-Lee J, Regan T, Shih BB, et al. Graphia: A platform for the graph-based visualisation and analysis of high dimensional data. *PLoS Comput Biol.* 2022;18(7):e1010310.

988 **Legends to Figures**

989 **Figure 1. *Il34* is widely-expressed in rat tissues but is not required for normal growth and**
990 **development.**

991 **(A)** The image shows mapping of RNA-seq reads from the rat atlas to the *Il34* locus. Each dot
992 represents read count from an individual tissue/library, colour coded based upon system as indicated.
993 The location on Chr19 (mRatBN7.2 assembly) is shown on the x axis*; Il34* is transcribed on the reverse
994 strand; the first coding exon at 38.729Mb is detected in libraries from all tissues (CDS exon 1). An
995 alternative non-coding exon at ca. 38.753Mb is detected primarily in libraries from mesenchymal
996 tissues (respiratory, cardiovascular, renal). The most distal 5' non-coding exon, at 38.764Mb, is
997 detected at low levels in multiple tissues. To the right of the image, reads are mapped to exons of the
998 upstream *Sf3b3* locus.

999 **(B)** Tibial bone density was measured by microCT in male and female rats at 8 weeks of age (BV/TV;
1000 Bone volume fraction, Tb.Th; trabecular thickness, Tb.N; trabecular number, TV; Total volume, Cort.
1001 Th; Cortical Thickness). Each dot represents an individual animal (n≥4).

1002 **(C)** Body weight gain. WT (blue) and *Il34*$^{-/-}$ (grey) rats were weighed when ear-notched (P12/P14), at
1003 weaning (P20/P21) and at P56. Each dot represents an independent animal.

1004 **(D&E)** Representative images of spleen morphology and distribution of macrophages in *Il34*$^{+/+}$ (upper
1005 panels) and *Il34*$^{-/-}$ (lower panels) rats. IBA1 staining (left) highlights the macrophages of the red pulp;
1006 and CD209b (right) the marginal zone macrophages.

1007 **(F)** Serum CSF1 was measured by ELISA. Each dot represents an individual animal.

1008 **(G)** Flow cytometric analysis of CD45R^{+} B and CD3^{+} T cells, granulocytes, HIS48^{+}(classical) and
1009 CD43^{+}(non-classical) monocytes from bone marrow, blood and spleen in 8 week old rats (n≥6). **(H)** *Ex*
1010 *vivo* imaging of diaphragm muscle and central tendon and the thymus isolated from *Il34*$^{+/+}$ and *Il34*$^{-/-}$
1011 animals carrying the *Csf1r*-mApple transgene. Tissues were directly imaged on an Olympus FV3000
1012 confocal microscope with a 10x objective and scalebar represents 100 μM.

1013 **Figure 2. Loss of IL34 reduces tissue resident macrophages in squamous epithelia and brain.**

1014 **(A)** Whole mount imaging of the epithelial layer of the ear, tongue, proximal oesophagus and foot
1015 from *Il34*$^{+/+}$ and *Il34*$^{-/-}$ animals carrying the *Csf1r*-mApple transgene. **(B)** Whole mount imaging of the
1016 mesothelium (surface), peritubular and interstitial regions of the testes. Tissues were directly imaged
1017 on an Olympus FV3000 confocal microscope with a 10x objective and scalebar represents 100 μM. **(C)**
1018 Half brains from *Il34*$^{+/+}$, *Il34*$^{+/-}$ and *Il34*$^{-/-}$ animals with the *Csf1r*-mApple reporter were homogenized
1019 into single cell suspension and analysed by flow cytometry. Total cells were enumerated after
1020 extraction and total numbers of microglia (CD45^{low}/Cd11b/c^{high}) and brain associated macrophages
1021 (BAM; CD45^{high}/CD11b/c^{low}) were calculated from proportions derived from flow cytometry.
1022 Representative plots from each genotype are shown and quantified, each dot represents an
1023 independent animal (n≥12).

1024 **Figure 3. Loss of IL34 leads to selective reduction of microglia in grey matter regions**

1025 **(A)** Representative images of brain sections stained for IBA1 (Green or Red) and DAPI (Blue) Images
1026 were captured on the Olympus FV3000 confocal microscope. Grey matter in cerebellum is demarcated
1027 by white dashed line. **(B)** Microglial density for each brain region (specifically grey matter in
1028 cerebellum) was quantified as described in Materials and Methods. Each point represents data from
1029 an individual animal. Statistical analysis was performed using a One-way ANOVA.

1030 **Figure 4. A gradient of microglial density and selective depletion of perivascular macrophages in**
1031 **grey matter of IL34-deficient rats**

1032 **(A)** Free floating sections of cortex from *Il34*$^{+/+}$, *Il34*$^{+/-}$ and *Il34*$^{-/-}$ brains stained with IBA1 (green) and
1033 DAPI (magenta). Panels show representative high resolution scans of the cortical layers from the
1034 meninges and cortical layer 1 (at top), through layer II-VI to the corpus callosum (CC) at bottom. Note
1035 the reduced density of IBA1^{+} cells in the CC (demarcated by white dotted line) and apparent gradient
1036 through the cortical layers. **(B-F)** CD163 (green) was used to identify perivascular macrophages (PVM).
1037 Representative images of thalamus and cerebellum grey matter (GM) from wildtype and *Il34*$^{-/-}$ **(B&C)**
1038 and whole cortical scans **(E)** are shown. White dashed lines demarcate the meninges and arrows

1039 indicate direction towards CC. Data are presented as percentage area stained with CD163 in different
1040 brain regions with each dot representing an independent animal and scalebars representing 100 µm.
1041 Statistical analysis was performed using a One-way ANOVA followed by Tukey's test.

1042 **Figure 5. Selective loss of the microglial gene signature in multiple brain regions in *Il34*$^{-/-}$ rats.**

1043 mRNA was isolated from cortex, hippocampus (hipp) and thalamus (thal) of 12 week old *Il34*$^{+/+}$ and
1044 *Il34*$^{-/-}$ rats (N=4/genotype) and gene expression was quantified by RNA-seq as described in Materials
1045 and Methods. Network analysis to identify co-expressed gene clusters was performed using Graphia.
1046 The complete dataset and cluster analysis in provided in Table S1. Cluster 18 is the only cluster showing
1047 a relationship with *Il34* genotype. **(A)** The average tag per million (TPM) count of all genes from cluster
1048 18 identified by network analysis is represented as a bar for each sample sequenced. **(B)** Each panel
1049 shows expression of individual genes from cluster 18; each dot represents an independent sample
1050 (n=4). **(C)** Representative images of cortex from adult *Il34*$^{+/+}$, *Il34*$^{+/-}$ and *Il34*$^{-/-}$ brains (n=3/genotype)
1051 stained with IBA1 (red) and TMEM119 (green). **(D)** Expression of genes encoding microglial
1052 transcription factors (*Pu.1, Irf5, Irf8* and *Sall1*) and macrophage markers (*Cd74 and Cd68*).

1053 **Figure 6. Loss of IL34 does not affect pathology in the adenine-diet induced model of chronic kidney**
1054 **disease.**

1055 Cohorts of male and female rats were fed normal chow or a diet containing 0.2% adenine for 6 weeks.
1056 **(A)** Animal body weights were measured over the period of the adenine diet. **(B)** Water consumption
1057 by cage was quantified by comparing the difference in the weights of the bottle to the prior day, each
1058 line represents a single cage tracked longitudinally and "F" denotes female cages. **(C)** Water
1059 consumption at the cage level for the 5th week of the diet, each dot represents an independent cage
1060 black dots are male cages and brown dots are female cages(n≥4). **(D&E)** Serum Creatinine and urea
1061 were measured from serum collected through cardiac puncture. **(F)** The number of crystals in each
1062 kidney was quantified by calculating the area of the crystal across the entire kidney and normalized to
1063 the size of the kidney section quantified. **(G)** Sirius red staining was quantified as total stained area
1064 over the entire area of the kidney section quantified.

1065 **Figure 7. IL34-dependent macrophage expansion during chronic kidney injury**

1066 Cohorts of male and female rats were fed normal chow or a diet containing 0.2% adenine were stained
1067 for IBA1 and CD163. **(A-C)** Representative images for IBA1 in the medulla and cortex **(A&B)** and CD163
1068 in the medulla **(C)** are shown. **(D&E)** Medulla and cortex from IBA1 stained kidneys were quantified as
1069 percentage of area stained. **(F)** CD163 was only detected and quantified in the medulla. Slides were
1070 scanned on an Olympus slide scanner (VS120 or VS200) with a 40x objective and images captured with
1071 the Olyvia software. Scale bars represent 50μM.

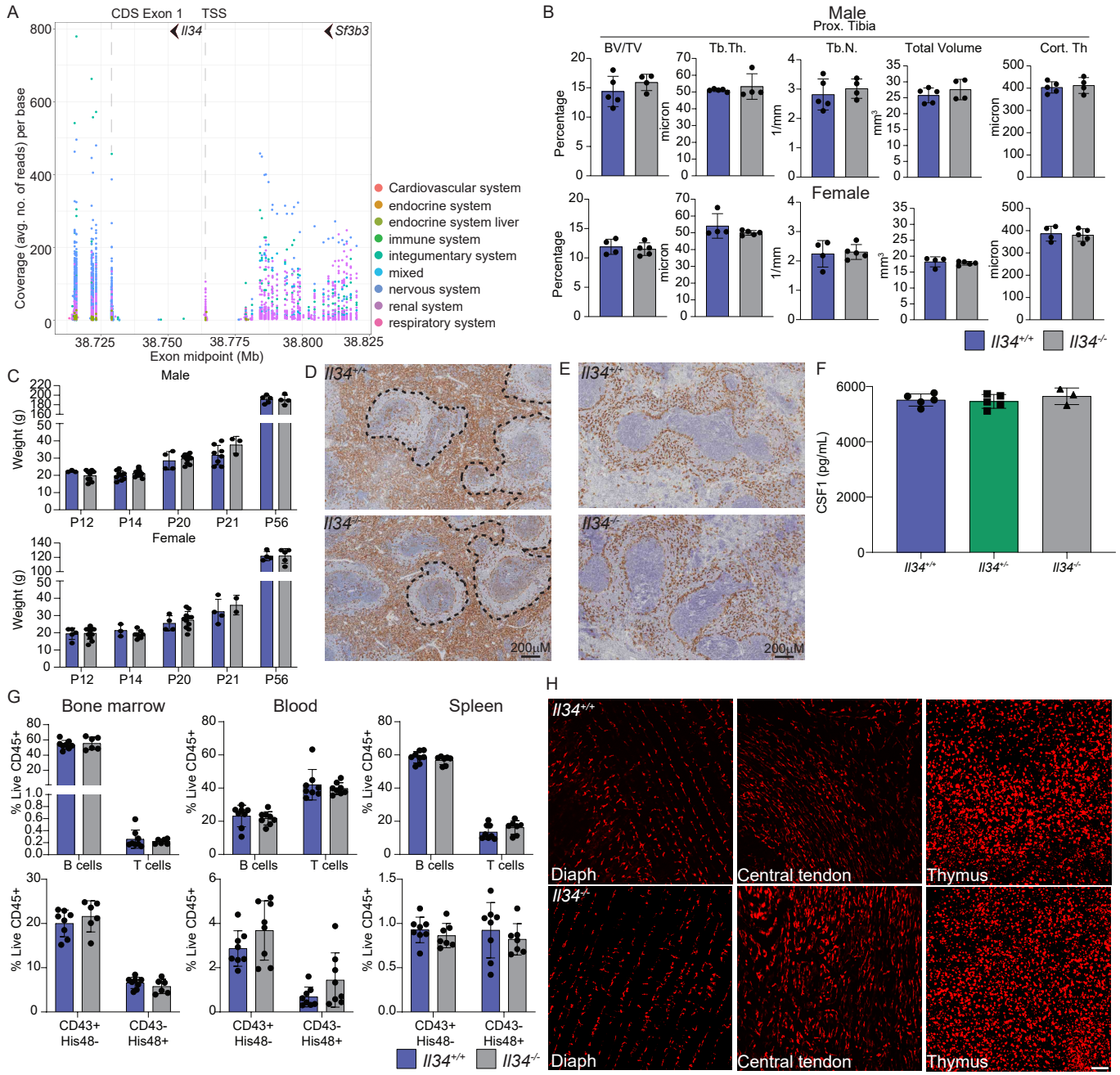
A
CDS Exon 1
TSS
Il34
Sf3b3
Coverage (avg. no. of reads) per base
Exon midpoint (Mb)
Cardiovascular system
endocrine system
endocrine system liver
immune system
integumentary system
mixed
nervous system
renal system
respiratory system
B
Male
Prox. Tibia
BV/TV
Tb.Th.
Tb.N.
Total Volume
Cort. Th
Percentage
micron
1/mm
mm³
Female
Il34+/+
Il34-/-
C
Male
Female
Weight (g)
P12
P14
P20
P21
P56
D
E
200µM
F
CSF1 (pg/mL)
Il34+/+
Il34+/-
Il34-/-
G
Bone marrow
Blood
Spleen
% Live CD45+
B cells
T cells
CD43+ His48-
CD43- His48+
H
Diaph
Central tendon
Thymus

Figure 1

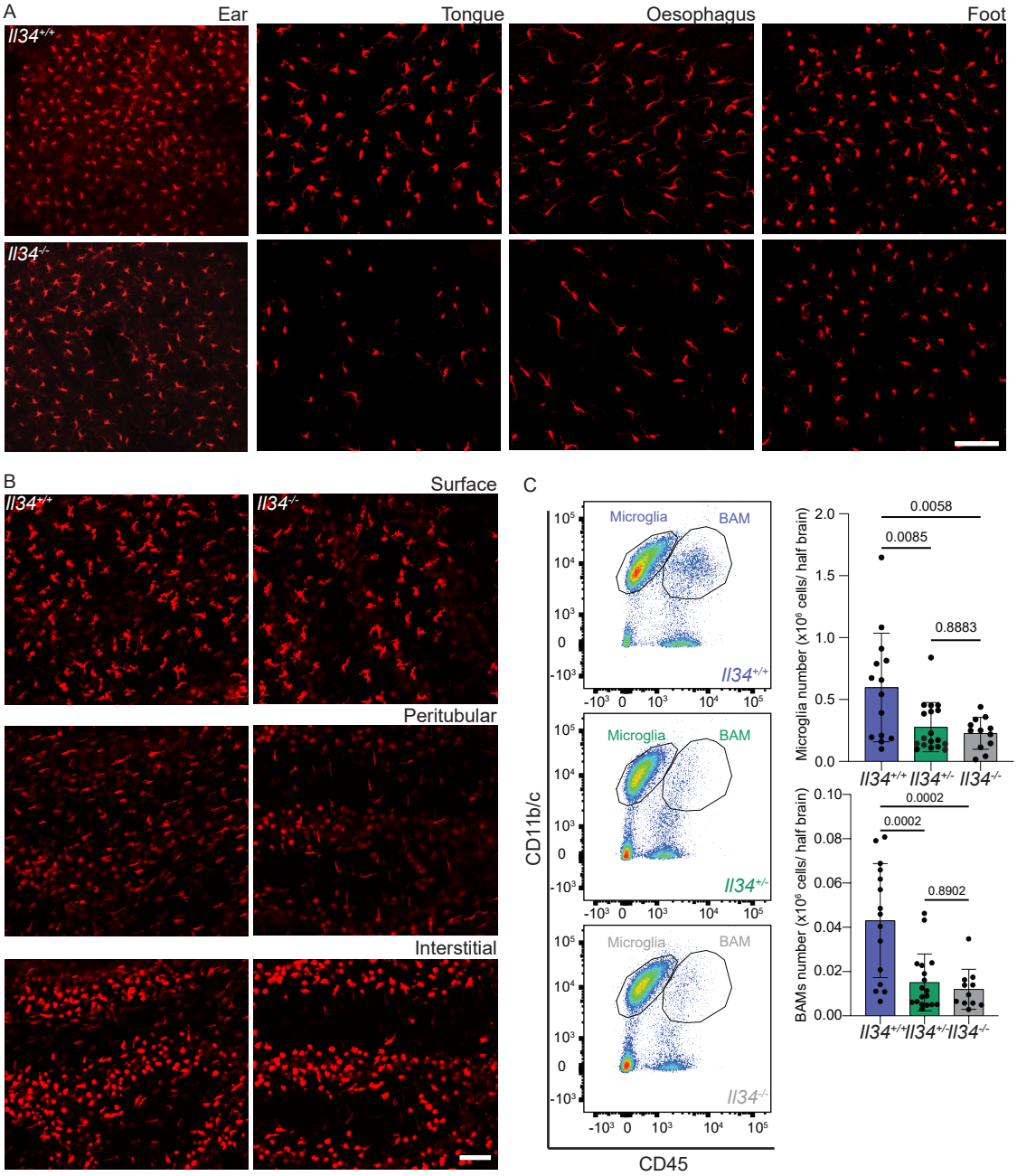
A
Ear
Tongue
Oesophagus
Foot
Il34+/+
Il34-/-
B
Surface
Peritubular
Interstitial
C
Microglia
BAM
CD11b/c
CD45
Il34+/+
Il34+/-
Il34-/-
Microglia number (x10^6 cells/ half brain)
BAMs number (x10^6 cells/ half brain)
0.0058
0.0085
0.8883
0.0002
0.0002
0.8902

Figure 2

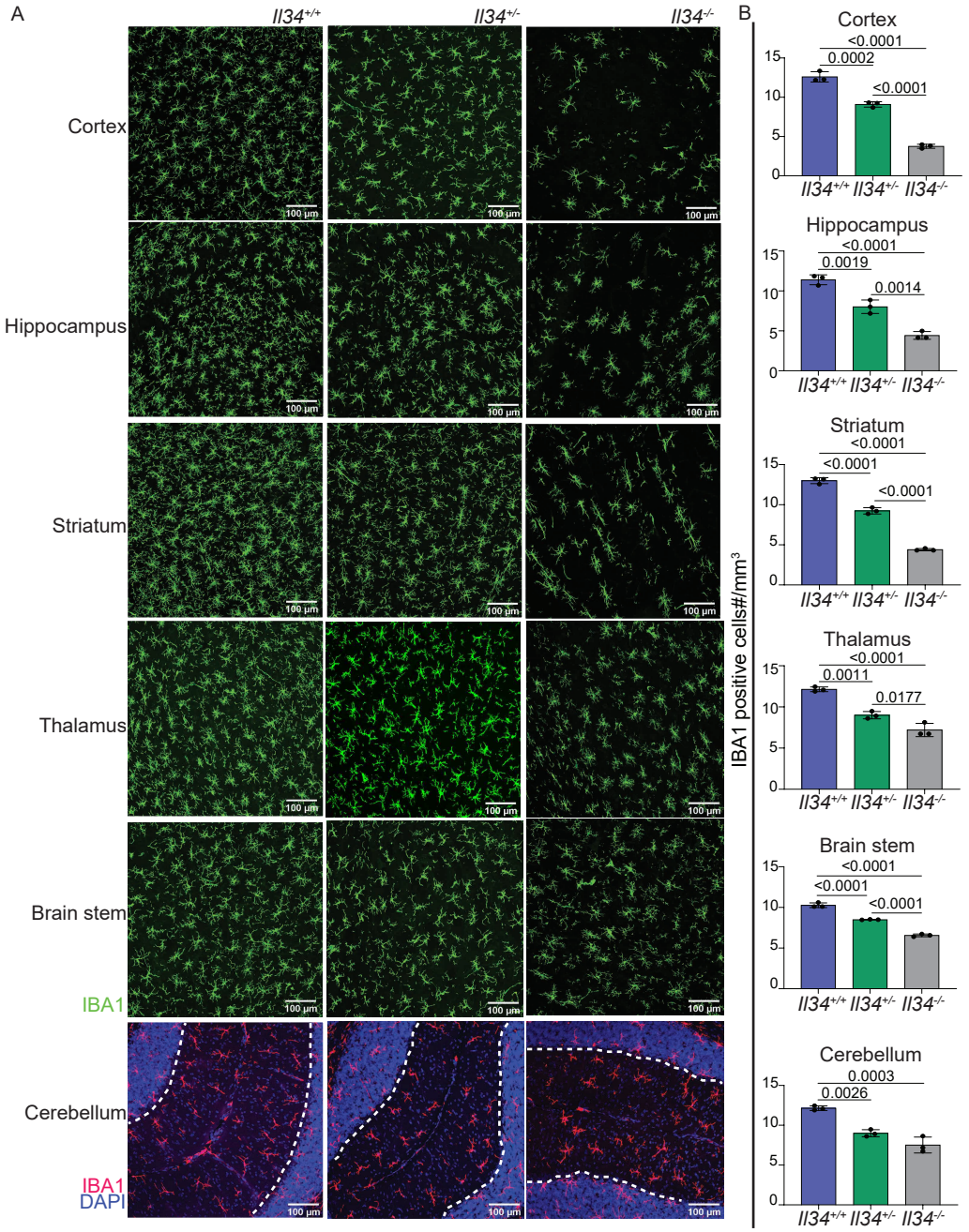
A
Il34+/+
Il34+/-
Il34-/-
Cortex
Hippocampus
Striatum
Thalamus
Brain stem
IBA1
Cerebellum
IBA1
DAPI
100 µm
B
IBA1 positive cells#/mm3
Cortex
<0.0001
0.0002
<0.0001
Hippocampus
<0.0001
0.0019
0.0014
Striatum
<0.0001
<0.0001
<0.0001
Thalamus
<0.0001
0.0011
0.0177
Brain stem
<0.0001
<0.0001
<0.0001
Cerebellum
0.0003
0.0026
Il34+/+ Il34+/- Il34-/-

Figure 3

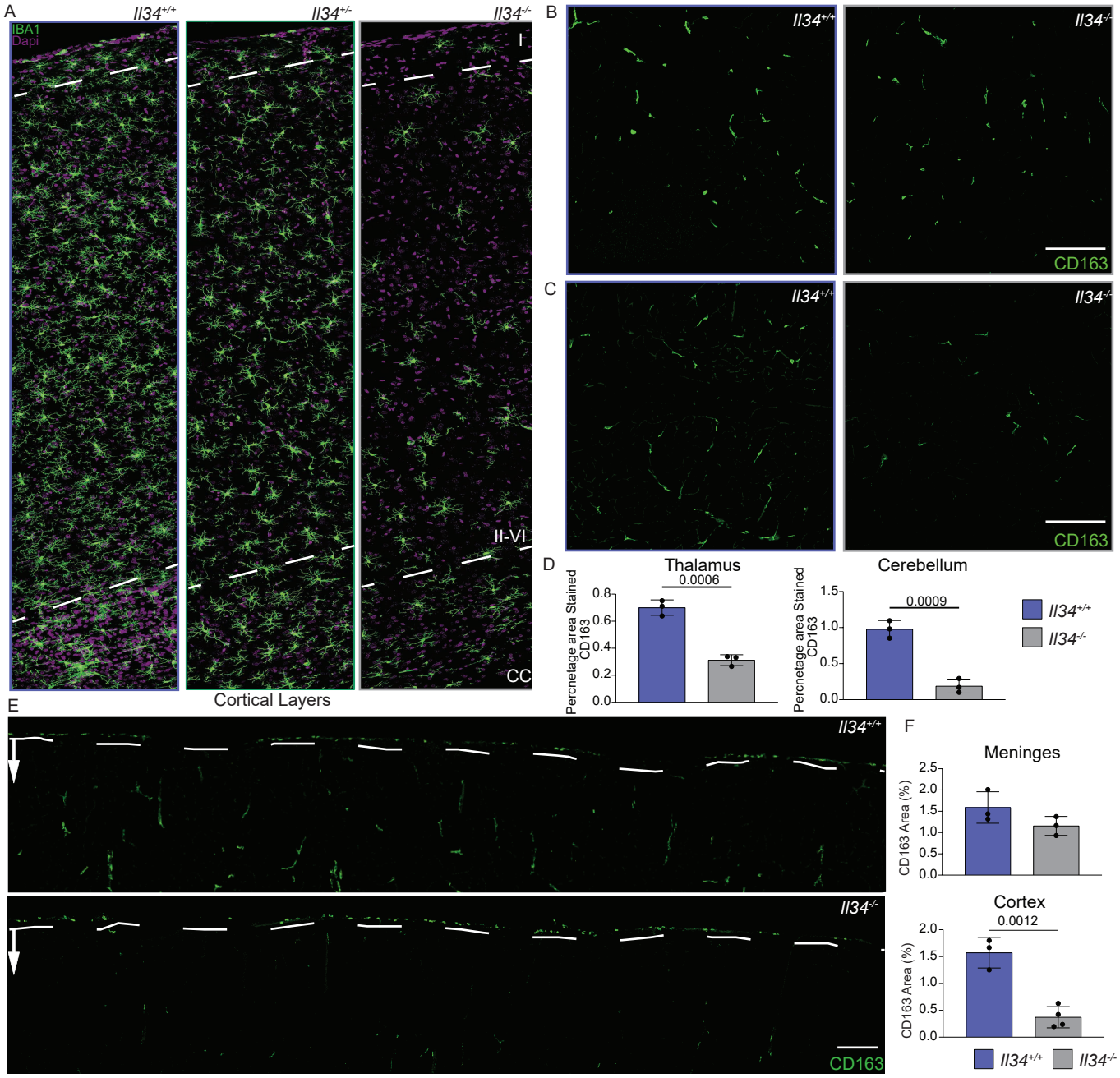
A
Il34+/+
Il34+/-
Il34-/-
IBA1
Dapi
I
II-VI
CC
Cortical Layers
B
Il34+/+
Il34-/-
CD163
C
Il34+/+
Il34-/-
CD163
D
Thalamus
0.0006
Percnetage area Stained CD163
0.8
0.6
0.4
0.2
0.0
Cerebellum
0.0009
Percnetage area Stained CD163
1.5
1.0
0.5
0.0
Il34+/+
Il34-/-
E
Il34+/+
Il34-/-
CD163
F
Meninges
CD163 Area (%)
2.5
2.0
1.5
1.0
0.5
0.0
Cortex
0.0012
CD163 Area (%)
2.0
1.5
1.0
0.5
0.0
Il34+/+
Il34-/-

Figure 4

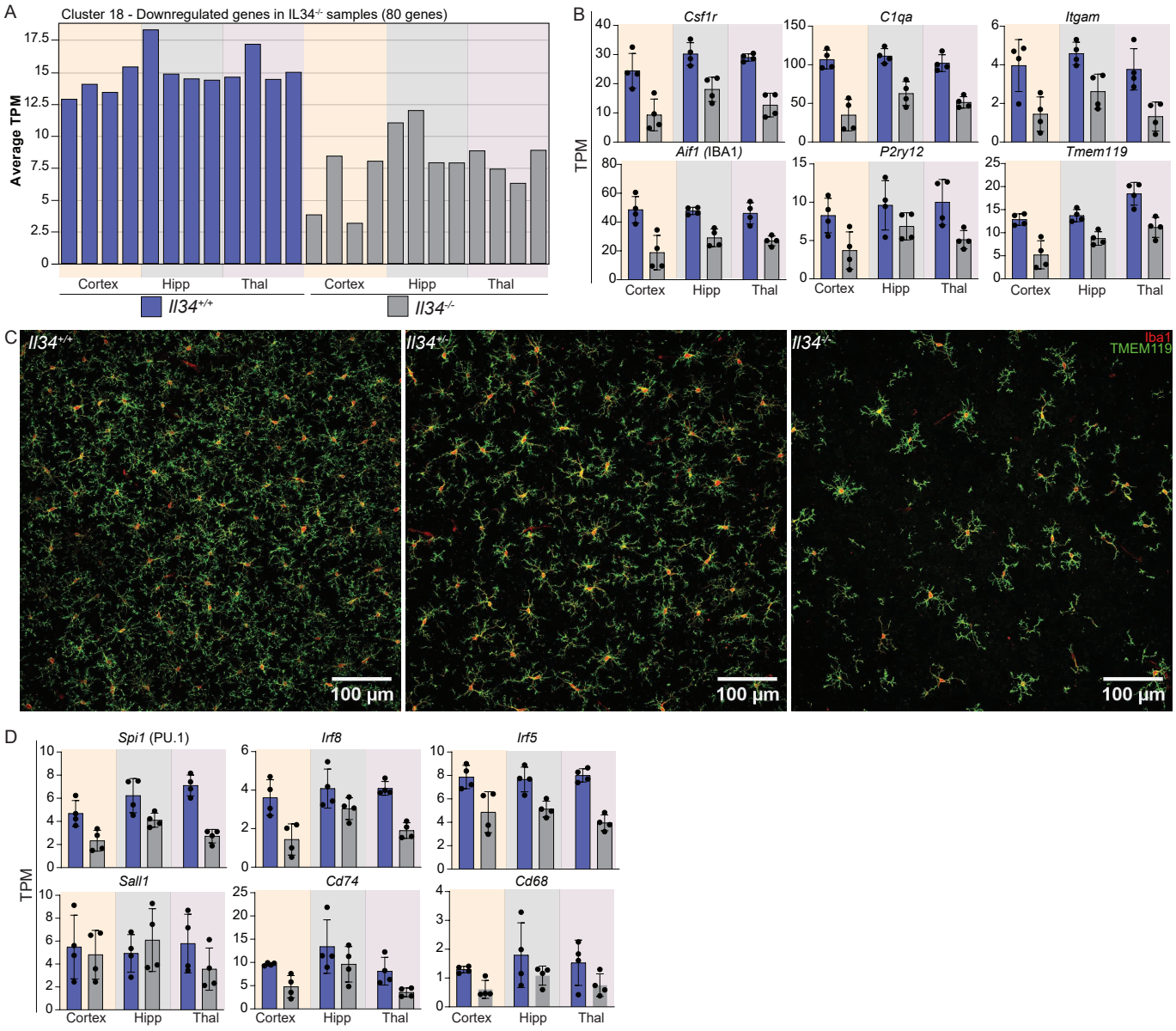
A
Cluster 18 - Downregulated genes in IL34-/- samples (80 genes)
Average TPM
Cortex
Hipp
Thal
Il34+/+
Il34-/-
B
Csf1r
C1qa
Itgam
Aif1 (IBA1)
P2ry12
Tmem119
TPM
C
Il34+/+
Il34+/-
Il34-/-
Iba1
TMEM119
100 µm
D
Spi1 (PU.1)
Irf8
Irf5
Sall1
Cd74
Cd68

Figure 5

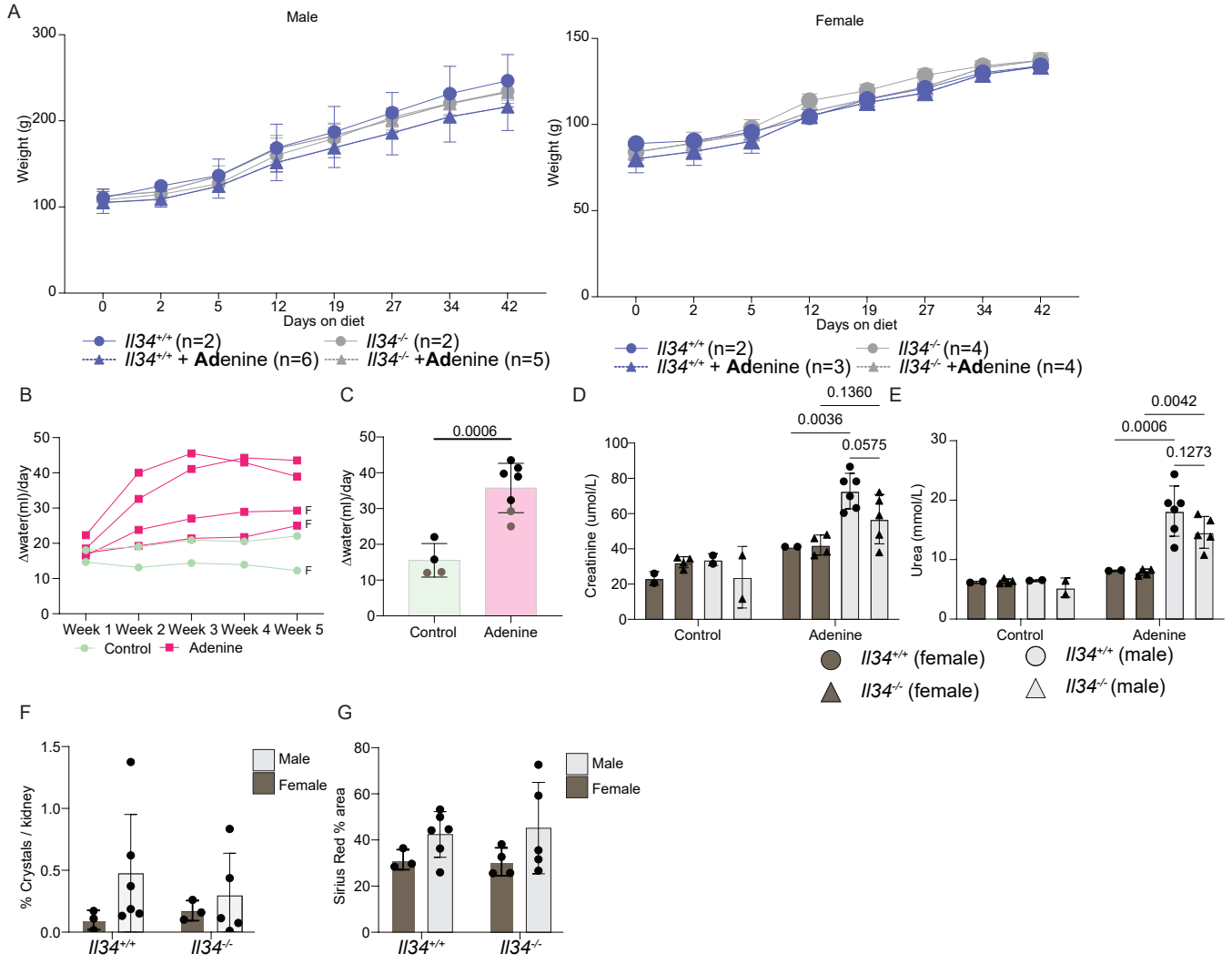
A
Male
Weight (g)
Days on diet
Il34+/+ (n=2)
Il34+/+ + Adenine (n=6)
Il34-/- (n=2)
Il34-/- +Adenine (n=5)
Female
Il34+/+ (n=2)
Il34+/+ + Adenine (n=3)
Il34-/- (n=4)
Il34-/- +Adenine (n=4)
B
Δwater(ml)/day
Week 1 Week 2 Week 3 Week 4 Week 5
Control
Adenine
C
0.0006
Control
Adenine
D
0.1360
0.0036
0.0575
Creatinine (umol/L)
E
0.0042
0.0006
0.1273
Urea (mmol/L)
Il34+/+ (female)
Il34-/- (female)
Il34+/+ (male)
Il34-/- (male)
F
% Crystals / kidney
Male
Female
G
Sirius Red % area

Figure 6

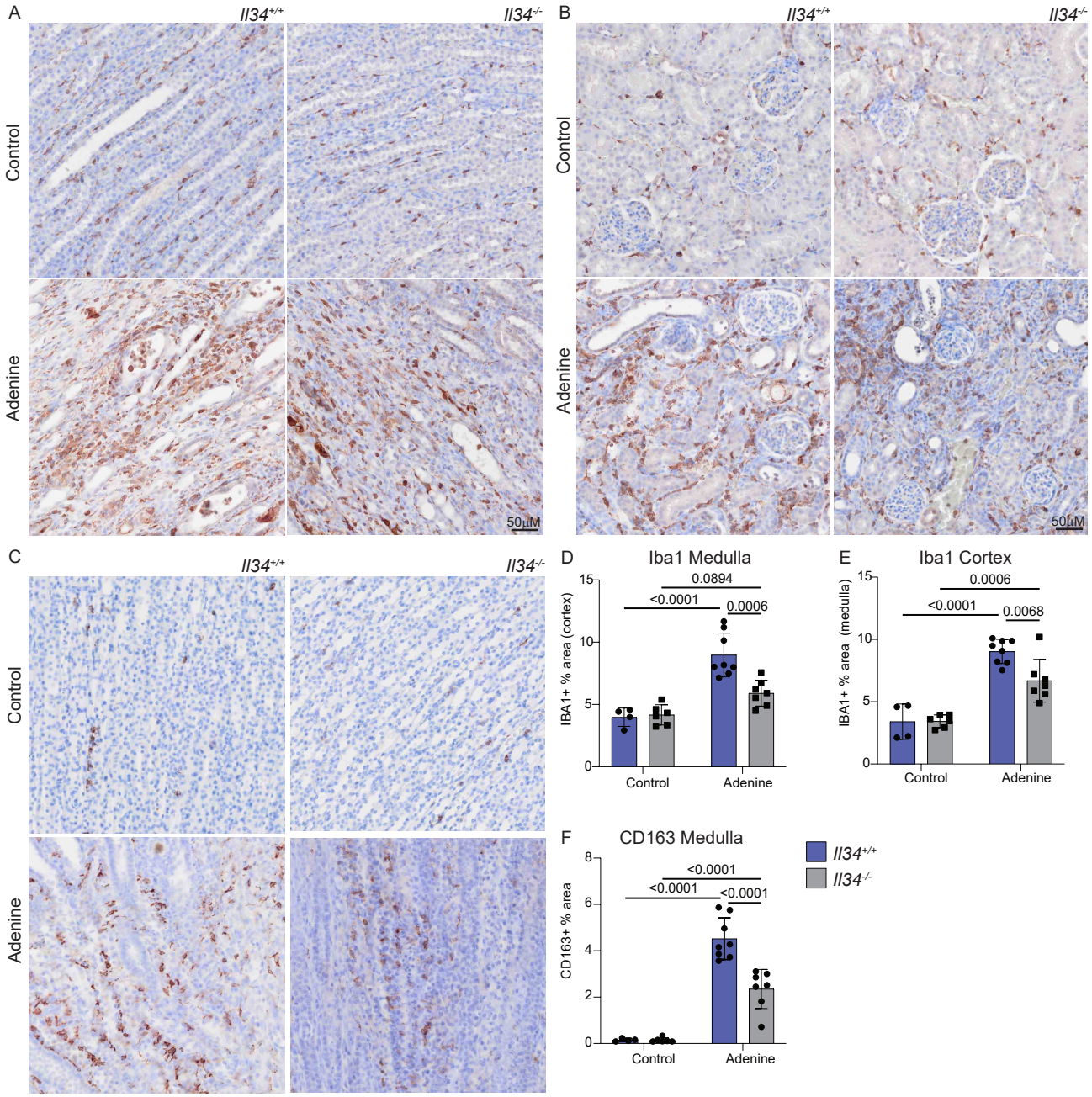
A
Il34+/+
Il34-/-
Control
Adenine
50µM
B
Il34+/+
Il34-/-
Control
Adenine
50µM
C
Il34+/+
Il34-/-
Control
Adenine
D
Iba1 Medulla
IBA1+ % area (cortex)
0.0894
<0.0001
0.0006
Control
Adenine
E
Iba1 Cortex
IBA1+ % area (medulla)
0.0006
<0.0001
0.0068
Control
Adenine
F
CD163 Medulla
CD163+ % area
<0.0001
<0.0001
<0.0001
Control
Adenine
Il34+/+
Il34-/-

Figure 7